Technical note: A comparative study of chemistry schemes for volcanic sulfur dioxide in Lagrangian transport simulations: a case study of the 2019 Raikoke eruption

Mingzhao Liu[1,2], Lars Hoffmann[1,2], Jens-Uwe Grooß[3,2], Zhongyin Cai[4], Sabine Grießbach[1,2], and Yi Heng[5]

[1]Jülich Supercomputing Centre, Forschungszentrum Jülich, Jülich, Germany
[2]Center for Advanced Simulation and Analytics (CASA), Forschungszentrum Jülich, Jülich, Germany
[3]Institute of Climate and Energy Systems, Stratosphere (ICE-4), Forschungszentrum Jülich, Jülich, Germany
[4]Yunnan Key Laboratory of International Rivers and Transboundary Eco-security, Institute of International Rivers and Eco-Security, Yunnan University, Kunming, China
[5]School of Computer Science and Engineering, Sun Yat-sen University, Guangzhou, China

Correspondence: Mingzhao Liu (mi.liu@fz-juelich.de)

Abstract. Lagrangian transport models are important tools to study the sources, spread, and ~~life time~~ lifetime of air pollutants. In order to simulate the transport of reactive atmospheric pollutants, the implementation of efficient chemistry and mixing schemes is necessary to properly represent the lifetime of chemical species. Based on a case study simulating long-range transport of volcanic sulfur dioxide (SO_2) for the 2019 Raikoke eruption, this study compares two chemistry schemes implemented in the Lagrangian transport model Massive-Parallel Trajectory Calculations (MPTRAC). The explicit scheme represents first-order and pseudo-first-order loss processes of SO_2 based on prescribed reaction rates and climatological oxidant fields, i. e., the hydroxyl radical in the gas phase and hydrogen peroxide in the aqueous phase. Furthermore, an implicit scheme with a reduced chemistry mechanism for volcanic SO_2 decomposition has been implemented, targeting the upper troposphere and lower stratosphere (UT/LS) region. Considering non-linear effects of the volcanic SO_2 chemistry in the UT/LS region, we found that the implicit solution yields a better representation of the volcanic SO_2 lifetime while the first-order explicit solution has better computational efficiency. By analysing the dependence between the oxidants and SO_2 concentrations, correction formulas are derived to adjust the oxidant fields used in the explicit solution, leading to a good trade-off between computational efficiency and accuracy. We consider this work to be an important step forward to support future research on emission source reconstruction involving non-linear chemical processes.

1 Introduction

Lagrangian transport models ~~calculate~~ simulate the trajectories of air parcels ~~carrying~~ that carry trace gases and aerosols ~~driven by external~~ through the atmosphere. These trajectories are determined using external datasets, which provide horizontal wind and vertical velocity fields obtained from meteorological reanalyses or forecast models. Lagrangian transport models are particularly useful for studying complex atmospheric processes, such as the interaction between different pollutants,

chemical transformations, and the influence of different meteorological conditions. Lagrangian transport models have been widely applied in studies of natural and ~~anthropogenic~~ anthropogenic pollutant emissions. Applications of Lagrangian models include the simulation of point source or regional pollutant emissions, such as volcanic eruptions (Webster and Thomson, 2022), nuclear leakage accidents (Stohl et al., 2012), or wildfires (Evangeliou et al., 2019). They can also be used for global chemical transport simulations and source estimations of greenhouse gases such as carbon dioxide (CO_2) or methane (CH_4) (Bergamaschi et al., 2022; Che et al., 2022), long-lived gases of chlorofluorocarbons (CFCs) or hydrofluorocarbons (HFCs) (Pommrich et al., 2014; Brunner et al., 2017), fossil emissions (Dalsøren et al., 2018), and more. In contrast to grid-based Eulerian models, which represent fluid transport at fixed grid locations and suffer from numerical diffusion due to limited grid resolution, trajectory-based Lagrangian models generally have much lower numerical diffusion. In addition, Lagrangian models have the specific advantage of high scalability and computational efficiency, making them suitable for long-range and large-scale simulations. When simulating a large number of chemical species, Lagrangian models do not need to calculate transport separately for each species as in a grid-based Eulerian scheme (Brunner, 2012). However, Lagrangian models can face challenges such as complex boundary condition handling, difficulties in representing concentration fields and physical diffusion, high particle requirements for dense regions and uneven computational loads.

In the past, Lagrangian models have often been used to qualitatively identify the source and reproduce the spatial distribution of plumes of trace gases, e. g., by tracking air parcels backward in time from receptors to sources to reconstruct the emissions (Wu et al., 2017; Pardini et al., 2017). In case studies of volcanic eruptions, usually the effects of SO_2 lifetime variations with altitude are neglected. However, Lagrangian models have the potential to be more quantitative. The essential step is to accurately model the physical and chemical processes for accurate prediction of the species lifetime. For atmospheric species such as SO_x, NO_x, hydrocarbons and halocarbons, the chemical reactions have a significant impact on estimating their sources and sinks. Uncertainties introduced by chemical sinks can strongly influence the top-down source estimation (Stavrakou et al., 2013).

In the Lagrangian framework, the motion of species is simplified to time integration along trajectories determined by meteorological data. ~~The modeling of species sinks is separated from the trajectory calculation and handled individually~~ Species sinks are modeled separately for each air parcel~~. Following a rigorous Lagrangian approach,~~, specifying the time derivative of the mass or mixing ratio of each species ~~is specified~~ with an explicit rate. This method can ~~model~~ represent processes such as dry/wet deposition, sedimentation, and first-order chemical reactions. For example, ~~in the study of Liu et al. (2023)~~, Liu et al. (2023) simulated the evolution of the SO_2 mass burden from the 2018 Ambae ~~volcanic eruption was simulated~~ eruption with explicit loss rates, including wet deposition, ~~gas phase and aqueous phase~~ gas-phase and aqueous-phase reactions, and discussed the height sensitivity of ~~the SO_2 loss rate, which is strongly~~ SO_2 loss rates related to cloud distributions~~, was discussed. To solve the~~. For bimolecular or second-order ~~chemical reactions, which~~ reactions, where rates depend on the ~~concentration of the species, the loss rates are expressed by prescribing the OH and H_2O_2 concentrations using a~~ concentrations of two species, Liu et al. (2023) prescribed monthly zonal mean ~~climatology~~ climatologies for OH and H_2O_2 to obtain pseudo first-order approximations for the SO_2 oxidation. However, ~~this approach is more suitable for simulating long-lived tracers at lower concentrations. In dense~~ in dense volcanic SO_2 plumes, ~~the OH and H_2O_2 concentrations decrease rapidly and may even~~

55 ~~be depleted by the reaction with SO_2. For more accurate simulations , these higher-order reactions should be considered~~ this approach may fail to capture oxidant depletion due to reactions with SO_2, particularly in regions of high SO_2 concentration. Accurate simulations under these conditions require dynamic coupling between reactant concentrations and reaction rates to properly represent second-order processes.

To model non-linear chemical processes, an implicit chemical solver and an atmospheric mixing scheme should be considered

60 (Brunner, 2012). In essence, while Lagrangian models efficiently track particle trajectories, a mixing scheme is essential to accurately represent diffusion and produce smooth gradients in concentration fields. Without a mixing scheme, particles carrying different reactants may remain isolated, resulting in pronounced local irregularities and inaccurate reaction rates. Mixing schemes address these issues by smoothing out irregularities in particle distributions, improving physical realism and ensuring numerical stability. In recent years, three main types of Lagrangian chemical and mixing schemes have been

65 considered. The first scheme uses a dynamically adaptive grid algorithm to mimic the stretching and distortion of air, such as in the Chemical Lagrangian Model of the Stratosphere (CLaMS) (McKenna et al., 2002b, a) and the Alfred Wegener InsTitute LAgrangian Chemistry/Transport System (ATLAS) (Wohltmann and Rex, 2009). The second scheme implements the chemistry scheme on a fixed 3-D grid, assuming uniform mixing of individual species within the grid boxes, such as in the U.K. Met Office's Next-Generation Atmospheric Dispersion Model (NAME) (Redington et al., 2009) and the Hybrid Single-

70 Particle Lagrangian Integrated Trajectory (HYSPLIT) (Stein et al., 2000) models. The third scheme implements the chemistry scheme on the Lagrangian air parcels, but uses a parameter to control the degree of mixing by adding a term to relax the trace gas concentrations in the air parcels to the background values averaged over a fixed 3-D grid, which is applied by the UK Meteorological Office (UKMO) chemistry transport model (STOCHEM) (Stevenson et al., 1998).

This paper focuses on the chemistry scheme implementation in the Lagrangian transport model Massive Parallel Trajectory

75 Calculations (MPTRAC) (Hoffmann et al., 2016, 2022). Here, we selected the third approach outlined above, as it allows for online coupling of chemistry calculations with trajectory calculations, performed separately for each air parcel, followed by inter-parcel mixing, making it particularly suitable for large-scale parallelization. MPTRAC is designed for large-scale atmospheric simulations on ~~HPC~~ High Performance Computing (HPC) systems and has a hybrid Message Passing Interface (MPI) - Open Multi-Processing (OpenMP) - Open Accelerator (OpenACC) parallelization scheme implemented, demonstrating

80 excellent performance and scalability on both CPUs (Liu et al., 2020) and GPUs (Hoffmann et al., 2024b). The model has been used in several case studies of simulating long-range transport of volcanic SO_2, with emission estimates obtained from a backward trajectory method (Wu et al., 2017, 2018; Cai et al., 2022) and a more complex and compute intensive inverse modeling approach (Heng et al., 2016). In those studies, the height-dependent lifetime of SO_2 was not considered as an influencing factor, since older versions of MPTRAC did not have a detailed chemistry scheme.

85 The main objective of this study is to introduce and assess a newly developed chemistry scheme with an implicit chemistry solver in the MPTRAC model, which improves long-range chemistry-transport simulations of volcanic SO_2 and allows for estimating the volcanic emission sources. We propose a small chemical mechanism with 12 species and 31 reactions to model the production and loss of OH, HO_2 and H_2O_2 in the UT/LS region, including reactions among $O(^1D)$, $O(^3P)$, H, OH, HO_2, O_3 and H_2O, together with reactions of SO_2 with OH in the gas phase and oxidation with H_2O_2 in the aqueous phase. The aim

90 is to model the dynamic OH and H_2O_2 fields as SO_2 oxidants to more realistically simulate and better represent the chemical lifetime of volcanic SO_2 in the UT/LS region. The chemical solver was built using the Kinetic Preprocessor (KPP) software package (Damian et al., 2002; Sandu and Sander, 2006). The KPP software provides a framework to automatically generate a Rosenbrock integrator for solving the stiff ordinary differential equations with specification of a chemical mechanism, including the chemical equations, species, and rate coefficients. The KPP has been widely used in atmospheric chemical modeling, for

95 instance in GEOS-CHEM (Henze et al., 2007) and MECCA (Sander et al., 2019).

In a case study, we conducted simulations of the June 2019 Raikoke volcanic eruption to compare and verify the modeled lifetime of the SO_2 emissions with TROPOspheric Monitoring Instrument (TROPOMI) satellite measurements (Veefkind et al., 2012; They) . The Raikoke (48.17°N, 152.15°E) eruption was a notable event that has been discussed in the literature to some larger extent. The eruption on 21-22 June was characterized by a series of explosive events that emitted SO_2 and volcanic ash into the

100 lower stratosphere, impacting the stratospheric aerosol layer (Gorkavyi et al., 2021; Kloss et al., 2021). Cai et al. (2022) used MPTRAC to estimate the SO_2 emissions and to investigate the effects of the injection height and time and of the diffusion parameters. With an estimated amount of (1.5 ± 0.2) Tg of SO_2, the eruption was notable for being the largest SO_2 injection into the upper troposphere and lower stratosphere since the 2011 Nabro eruption (Cai et al., 2022). de Leeuw et al. (2021) discuss the transport and chemical evolution of SO_2 emissions resulting from the 2019 Raikoke eruption, offering a comprehensive

105 comparison between NAME model simulations and TROPOMI observations.

The paper is organized as follows. In Sect. 2, we introduce the MPTRAC model, including the details of the implementation of the chemistry schemes, and the TROPOMI SO_2 satellite data set. In Sect. 3, we discuss the results of the Lagrangian chemical transport simulations with MPTRAC for the Raikoke eruption, including the evaluation of the modeled SO_2 fields in the UT/LS region with the satellite data. Finally, Sect. 4 provides the summary and conclusions of the study.

2 Data and methods

2.1 Overview on the MPTRAC model

Massive-Parallel Trajectory Calculations (MPTRAC) is a Lagrangian transport model, which is designed for heterogeneous CPU/GPU HPC systems and particularly suitable for large-scale and long-term atmospheric simulations in the free troposphere and stratosphere (Hoffmann et al., 2016, 2022). The model requires meteorological input fields, in particular the horizontal

115 wind and vertical velocity fields for the kinematic trajectory calculations, the temperature field for the chemistry calculations and the cloud water fields for wet deposition and aqueous phase chemistry. The trajectories of the air parcels are calculated by using the explicit mid-point method to maintain the balance between computational efficiency and accuracy (Rößler et al., 2018). Following Stohl et al. (2005), diffusion is represented via stochastic perturbations added to the position of the air parcels and subgrid-scale wind fluctuations are modelled modeled as a Markov process using the Langevin equation.

120 Unresolved convection is modeled via the extreme convection parametrization (Gerbig et al., 2003; Hoffmann et al., 2023). A comprehensive description of the model is given by Hoffmann et al. (2022). In the following section, we will discuss the two chemistry schemes implemented in the model in more detail.

Lagrangian transport simulations with MPTRAC are driven by global meteorological reanalyses or forecasts. Here, we applied the European Centre for Medium-Range Weather Forecasts' (ECMWF's) fifth generation reanalysis ERA5 (Hersbach et al., 2020), which provides hourly meteorological data at $0.3° \times 0.3°$ horizontal resolution on 137 vertical levels from the surface up to 0.01 hPa. Utilizing a state-of-the-art data assimilation system, ERA5 integrates a vast array of historical observations, including satellite and in-situ data, to generate consistent, accurate, and temporally continuous records of ~~meteorological~~ meteorological information from the year 1950 to the present. The ERA5 data provide significant improvements in meteorological information compared to the previous generation ERA-Interim reanalysis (Dee et al., 2011), which benefits the accuracy of Lagrangian transport simulations (Hoffmann et al., 2019).

2.2 Chemistry schemes and mixing in MPTRAC

2.2.1 First-order explicit chemistry scheme

In a Lagrangian model, linear decay processes over time t can be expressed as

$$\frac{dy}{dt} = ky, \tag{1}$$

where y represents the mass or volume mixing ratio (VMR) of a species in an air parcel. For a constant loss rate k, this ordinary differential equation is solved explicitly using the exponential equation,

$$y(t + \Delta t) = y(t)e^{-k\Delta t}. \tag{2}$$

Here, the rate coefficient k is prescribed as a model input. In MPTRAC, various loss processes such as wet/dry deposition or sedimentation are ~~modelled~~ modeled in this way. When solving first-order chemical reactions, e. g., photolysis, the explicit solution has good computational efficiency as it does not require numerical integration. The reactions of long-lived tracers with short-lived radicals can also be treated as pseudo-first-order reactions, assuming that production and loss of the radicals are in equilibrium and the pseudo-first-order rate constant k can be expressed as the product of the second-order rate coefficient k_{2nd} with the concentration of the oxidant, $k = k_{2nd}[X]$.

In MPTRAC, prescribed radical species concentrations are taken from a monthly zonal mean climatology of Pommrich et al. (2014), which has been prepared with the CLaMS model. In contrast to MPTRAC, which focuses on efficient particle transport with limited or simplified chemistry, the CLaMS model emphasizes detailed chemical reaction schemes for stratospheric processes. We consider the CLaMS model a reliable source for creating radical species climatologies for the UT/LS region. Following Liu et al. (2023), the OH field is scaled with a correction factor based on the solar zenith angle to mimic diurnal variations while preserving daily averages. Similarly, the monthly zonal mean H_2O_2 background field was obtained from the Copernicus Atmosphere Monitoring Service (CAMS) reanalysis (Inness et al., 2019) compiled into a monthly zonal mean climatology. At each time step, background field values are interpolated from the tabulated zonal mean data according to the pressure and latitude of the air parcels.

Regarding the SO_2 chemical reactions, the gas phase oxidation with OH and the aqueous phase oxidation with H_2O_2 are considered. In the cloud aqueous phase, H_2O_2 oxidation is the predominant pathway when pH<5 (Seinfeld and Pandis, 2016;
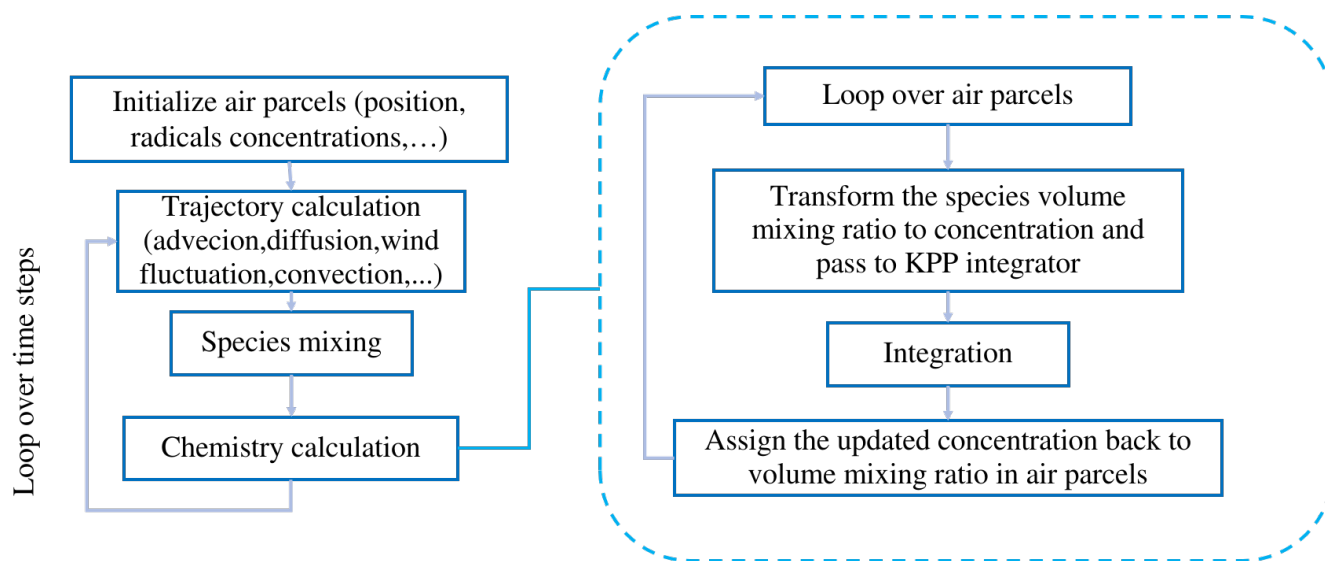
Figure 1. Simplified flow chart of the Massive-Parallel Trajectory Calculations (MPTRAC) Lagrangian chemistry-transport model.

155   Rolph et al., 1992; Pattantyus et al., 2018). Other aqueous phase oxidation pathways such as ozone oxidation and catalyzed oxidation via Fe(III) and Mn(II) are neglected because of low pH values in highly concentrated SO_2 volcanic plumes. Liu et al. (2023) conducted a case study of the 2018 Ambae eruption with the first-order simplified chemistry scheme of MPTRAC, which provides more details.

2.2.2   Implicit chemistry scheme

160   ~~A~~ Figure 1 shows a simplified flow chart of the ~~chemistry implementation in MPTRAC is shown in Fig. 1~~MPTRAC model, including details of the chemistry calculations. The chemistry ~~calculation~~ calculations follows the trajectory calculations and the mixing process. At each chemistry time step, the species VMRs of each air parcel are multiplied by the molecular density of air to convert them into concentration units (molecules/cm^3). After numerical integration of the chemical mechanism with the KPP integrator, the updated concentrations evolved in time are converted back to VMRs and assigned back to each air parcel.

165   The chemical processes of different air parcels are calculated independently of each other, making this an ~~embarrassingly~~ ideal parallel compute problem, which is particularly suitable for parallelization.

     Our proposed chemistry mechanism for the decomposition of volcanic SO_2 in the UT/LS region includes 31 reactions and 12 species, detailed in Table 1. This ~~mechanism models the dynamic production and loss of the OH and H_2O_2 concentration to further simulate SO_2 oxidation in both gas and aqueous phases~~specific mechanism is newly proposed and has not been

170   published or evaluated elsewhere. We developed the mechanism starting from SO_2 oxidation via OH in the gas phase (R31) and oxidation via H_2O_2 in the aqueous phase (R30), which are the major loss mechanisms ~~(Pattantyus et al., 2018; Rolph et al., 1992)~~ ~~. OH production~~ for volcanic SO_2 (Rolph et al., 1992; Pattantyus et al., 2018; de Leeuw et al., 2021). Next, we integrated further reactions to model the dynamic production and loss of OH and H_2O_2.

Table 1. Proposed chemistry scheme for volcanic SO_2 oxidation in the UT/LS region.

Index	Reaction
R1	$O(^3P) + O_2 \longrightarrow O_3$
R2	$O(^3P) + O_3 \longrightarrow 2\,O_2$
R3	$O(^3P) + OH \longrightarrow O_2 + H$
R4	$O(^3P) + HO_2 \longrightarrow OH + O_2$
R5	$O(^3P) + H_2O_2 \longrightarrow OH + HO2$
R6	$O(^1D) + O_2 \longrightarrow O(^3P) + O_2$
R7	$O(^1D) + O_3 \longrightarrow 2\,O(^3P) + O_2$
R8	$O(^1D) + H_2 \longrightarrow OH + H$
R9	$O(^1D) + H_2O \longrightarrow 2\,OH$
R10	$O(^1D) + N_2 \longrightarrow O(^3P) + N_2$
R11	$O(^1D) + N_2 \longrightarrow N_2O$
R12	$O(^1D) + N_2O \longrightarrow$ ~~prod~~ products
R13	$H + O_2 \longrightarrow HO_2$
R14	$H + O_3 \longrightarrow OH + O_2$
R15	$H + HO_2 \longrightarrow 2\,OH$
R16	$H + HO_2 \longrightarrow O(^3P) + H_2O$

Index	Reaction
R17	$H + HO_2 \longrightarrow H_2 + O_2$
R18	$OH + O_3 \longrightarrow HO_2 + O_2$
R19	$OH + OH \longrightarrow H_2O + O(^3p)$
R20	$OH + OH \longrightarrow H_2O_2$
R21	$OH + HO_2 \longrightarrow H_2O + O_2$
R22	$OH + H_2O_2 \longrightarrow H_2O + HO_2$
R23	$HO_2 + O_3 \longrightarrow OH + 2\,O_2$
R24	$HO_2 + HO_2 \longrightarrow O_2 + H_2O_2$
R25	$O_2 + h\nu \longrightarrow 2\,O(^3P)$
R26	$O_3 + h\nu \longrightarrow O(^1D) + O2$
R27	$O_3 + h\nu \longrightarrow O(^3P) + O_2$
R28	$H_2O + h\nu \longrightarrow H + OH$
R29	$H_2O_2 + h\nu \longrightarrow 2\,OH$
R30	$SO_2 + H_2O_2(aq) \longrightarrow$ ~~prod~~ products
R31	$SO_2 + OH \longrightarrow$ ~~prod~~ products

The production of OH mainly occurs via the reaction of H_2O with the excited oxygen radical $O(^1D)$ (~~Reaction~~ R9). ~~Its~~
The OH concentration exhibits a clear diurnal variation due to the strong relationship with solar radiation (R25 – R29) and photolysis, and its short lifetime from self-reaction (R19 and R20) and reactions with O_3 (~~Reaction R9~~ R18) and HO_2 (~~Reaction~~ R21) (Minschwaner et al., 2011; Tan et al., 2019). The H_2O_2 is primarily formed through the self-reaction of hydroperoxy radicals (HO_2) (~~Reaction~~ R24), which are mainly produced via H and O_2 ~~(Rieger et al., 2018).~~ (R13) (Rieger et al., 2018). We incorporated additional reactions into the chemical mechanism, even though they are less relevant to the primary focus of volcanic SO_2 decomposition in the UT/LS, to capture potential secondary effects that might influence the system under certain conditions or improve applicability.

Note that this scheme for the oxidation of SO_2 was not designed for application in the boundary layer and lower troposphere, as it excludes nitrogen oxides ~~(NOx)~~, hydrocarbons, and carbon monoxide emissions and reactions. Furthermore, to simplify and constrain the chemistry calculations, each air parcel's ozone VMR is updated at every chemistry time step using ERA5 reanalysis data interpolation. Water vapor is also updated using ERA5 reanalysis data. The rate coefficients of all chemical reactions were taken from the current recommendations of Burkholder et al. (2019).

For photolysis modeling, we created 3-D photolysis rate look-up tables for the different species, $J = J(\theta_s, \text{TCO}, p)$, where θ_s is the solar zenith angle, TCO is total column ozone, and p is pressure. The photolysis rate look-up tables cover 33 solar zenith angles from 0 to 96°, 8 total column ozone levels from 100 to 450 DU, and 66 pressure levels from 1013.25 to 0.1 hPa. The

look-up tables were generated using the DISSOC photolysis module of CLaMS, originally based on Lary and Pyle (1991) and improved over time in several studies (Becker et al., 2000; Hoppe et al., 2014; Pommrich et al., 2014). Note that for the DISSOC photochemistry model, we established the relationship between pressure, temperature, and ozone density via the U.S. Standard Atmosphere, 1976. The MPTRAC chemistry code determines θ_s, TCO, and p for each air parcel and linearly interpolates the corresponding J values from the look-up tables. The look-up table approach has the advantages of high computational efficiency and easy implementation on both GPUs and CPUs.

2.3 Wet deposition

Although the primary focus of this study is the comparison between the explicit and implicit chemistry schemes, it is also important to briefly outline the treatment of wet deposition in the MPTRAC model, as this is another significant loss process for volcanic SO_2 in cloud-containing environments. Wet deposition refers to the removal of SO_2 through processes such as precipitation scavenging, where SO_2 is dissolved in water droplets or ice crystals and subsequently removed from the atmosphere. Although the focus of this study is on chemical losses, it is crucial to consider wet deposition, particularly in tropical regions or during eruptions with high levels of atmospheric moisture, as it can significantly influence the lifetime of SO_2 and its transport in volcanic plumes. The interplay between wet deposition and chemical reactions in the presence of clouds contributes to the overall removal of SO_2 from the atmosphere, which is essential for accurate modeling of volcanic emissions and their impact on atmospheric chemistry.

In MPTRAC, wet deposition is implemented as a first-order loss term, where the removal rate of SO_2 depends on its concentration in the air parcel and the cloud water content. The in-cloud wet deposition rate is modeled via a rain-out process that considers the solubility of SO_2 and the precipitation rate, while the below-cloud deposition is represented by an empirical exponential formula based on precipitation intensity. This framework enables the model to account for the effects of cloud coverage and precipitation on SO_2 removal in both, gas and aqueous phase. The methodology for wet deposition in MPTRAC is detailed in Hoffmann et al. (2022) and has been modified and extended to address volcanic SO_2 deposition in Liu et al. (2023) . Wet deposition has been considered in all simulations discussed in this paper.

2.3.1 Inter-parcel mixing algorithm

~~Atmospheric~~ As mentioned in the introduction, atmospheric mixing is particularly important for properly modeling chemistry and transport in Lagrangian models (Brunner, 2012). The Lagrangian method inherently avoids numerical diffusion. A parametrisation of mixing needs to be included to simulate transport and chemistry in realistic manners. Here, we adapted the inter-parcel mixing scheme of Collins et al. (1997). This mixing scheme has the advantage of simple implementation and being well suited to CPU and GPU parallelization.

Following Collins et al. (1997), a relaxation term $d(c - \bar{c})$ is added to bring the VMR value c of each air parcel closer to the average value $\bar{c}$ within fixed grid boxes. A mixing parameter of $d = 0$ means there is no mixing whereas a mixing parameter of $d = 1$ means the species VMR is fully relaxed to the grid box mean. The parameter d therefore controls the degree of mixing. Default values of d are taken from Stevenson et al. (1998) to be 10^{-3} in the troposphere and 10^{-6} in the stratosphere. The grid

box size was set to $5° \times 5° \times 1\,km$ (longitude $\times$ latitude $\times$ log-pressure height). Mixing was conducted at every time step of the model, which is 180 s in this case.

2.4 TROPOMI SO$_2$ observations

In order to validate the simulated volcanic SO$_2$ distributions and lifetime for the Raikoke eruption, we used the Tropospheric Monitoring Instrument (TROPOMI) SO$_2$ Level 2 data product (Veefkind et al., 2012; Theys et al., 2017). TROPOMI is an ultraviolet, visible, near and short-wavelength infrared spectrometer. It is mounted on ~~ESA~~the European Space Agency's Sentinel-5P satellite. The satellite operates in a near-polar Sun-synchronous orbit with a local time of 13:30 for the ascending nodes. TROPOMI samples the Earth's surface and atmosphere with a spatial resolution of $7 \times 3.5\,km^2$ over a swath width of 2600 km. TROPOMI monitors ozone, methane, formaldehyde, aerosol, carbon monoxide, NO$_2$ and SO$_2$ in the atmosphere.

The TROPOMI Level 2 data include three SO$_2$ data products that provide SO$_2$ total column densities derived assuming a 1 km deep SO$_2$ layer centered at 1, 7, and 15 km of altitude. In this study, we used the 15 km product because it best fits the SO$_2$ mass release from Raikoke volcano into the UT/LS region. To obtain the SO$_2$ total mass burden, we first averaged the TROPOMI retrieval data over horizontal grid boxes of $0.1° \times 0.1°$ and then integrated the averaged values of the grid boxes. Note that the TROPOMI SO$_2$ total column data are provided in units of Dobson Units (DU). This is similar to ozone measurements, but for SO$_2$, 1 DU corresponds to a total column density of $2.85 \cdot 10^{-5}\,kg\,m^2$. A lower bound of 0.35 DU was applied to both the satellite measurements and the model results to reduce the effect of noise from the satellite measurements and to improve comparisons.

3 Results of the Raikoke case study

3.1 Model initialization and ~~setup~~baseline simulation

In an earlier study, Cai et al. (2022) ~~investigate~~ investigated the time- and height-resolved SO$_2$ injection parameters of the 2019 Raikoke eruption based on a backward-trajectory approach and SO$_2$ retrievals from TROPOMI observations. In this work, we used the same estimates of the SO$_2$ injections as Cai et al. (2022) to initialize the release of air parcels in the transport simulations. A total SO$_2$ mass of 1.6 Tg was distributed over 10^6 air parcels. The main injection peak occurs between June 21 and 22, 2019, at altitudes between 5 and 15 km. The vertical profile of the SO$_2$ injection rates is shown in Fig. 2. ~~Two numerical~~ Numerical experiments were conducted with MPTRAC to compare the results of the linear explicit and non-linear implicit chemistry solutions. Here, the simplified explicit approximation scheme is similar to the work in Liu et al. (2023), considering the gas phase oxidation and aqueous phase oxidation with climatological background OH and H$_2$O$_2$ fields as introduced in Sect. 2.2.1. The KPP implicit solution considers the same reactions of SO$_2$, but the OH and H$_2$O$_2$ fields are modeled with the chemical mechanism listed in Table 1.

The simulated SO$_2$ plume evolution with the KPP implicit chemistry scheme is compared with TROPOMI observations in Figs. 3 and 4. ~~From~~ The explicit scheme closely matches the implicit scheme in plume shape (not shown) but shows overall
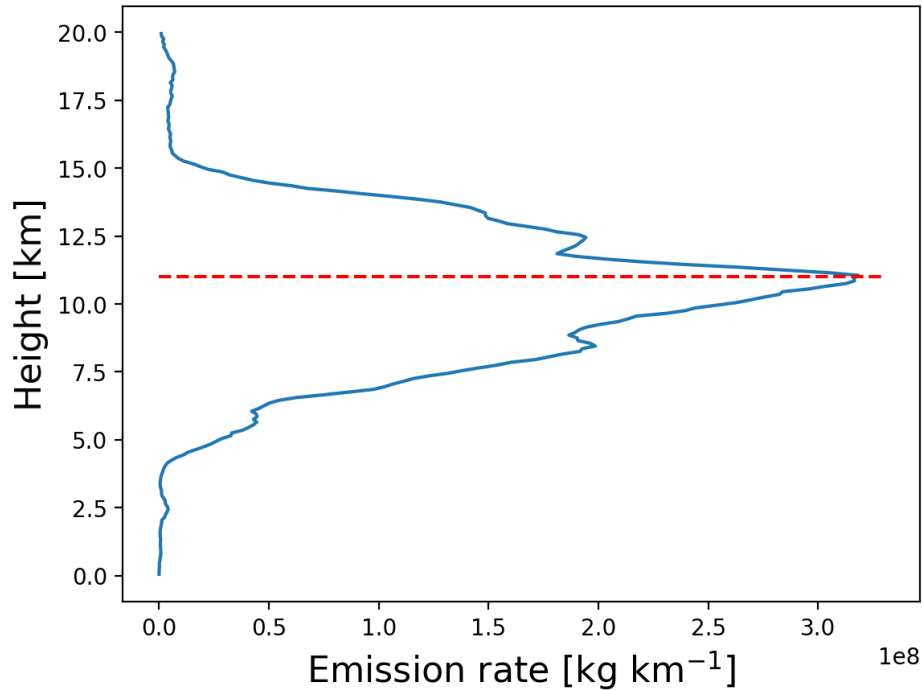
Figure 2. Vertical profile of SO$_2$ injections of the Raikoke eruption as estimated by Cai et al. (2022). The red line represents the tropopause height at the location of the volcano.

lower SO$_2$ column densities due to higher OH oxidation loss rates. Based on these comparisons, ~~it is found that~~ the MPTRAC model ~~captures the overall distribution and movement~~ effectively captures the dispersion and transport of the volcanic SO$_2$ plume ~~well~~ during the first 10 days after the eruption. Both the TROPOMI retrievals and the MPTRAC simulations show that the SO$_2$ plume continuously spreads over a larger area, with significant eastward motion and following the cyclonic flows. ~~Similar to the studies~~ Consistent with the findings of Cai et al. (2022) and ~~(de Leeuw et al., 2021)~~de Leeuw et al. (2021), the model results ~~begin to~~ gradually lose the ability to capture ~~some~~ certain structural features of the observed SO$_2$ distributions ~~and show a stronger diffusion effect due~~ after the first few days. This decline is attributed to the limited resolution of the meteorological data~~after the first few days, but~~, which also leads to a stronger diffusion effect. Nevertheless, the overall propagation direction and ~~the dispersion regions still remain consistent~~dispersion regions remain well-aligned with observations. In this paper, we will focus on the analysis of the volcanic SO$_2$ mass evolution and chemical lifetime based on this baseline simulation.

3.2 SO$_2$ chemical lifetime analysis

The time evolution of the total SO$_2$ mass burden of the 2019 Raikoke eruption from the MPTRAC simulations and TROPOMI observations is shown in Fig. 5a. The total mass burdens from the model and the observations were obtained by integrating the SO$_2$ column densities on a $0.1° \times 0.1°$ horizontal grid. For ~~comparison with~~this comparison, the satellite data ~~,~~and the grid
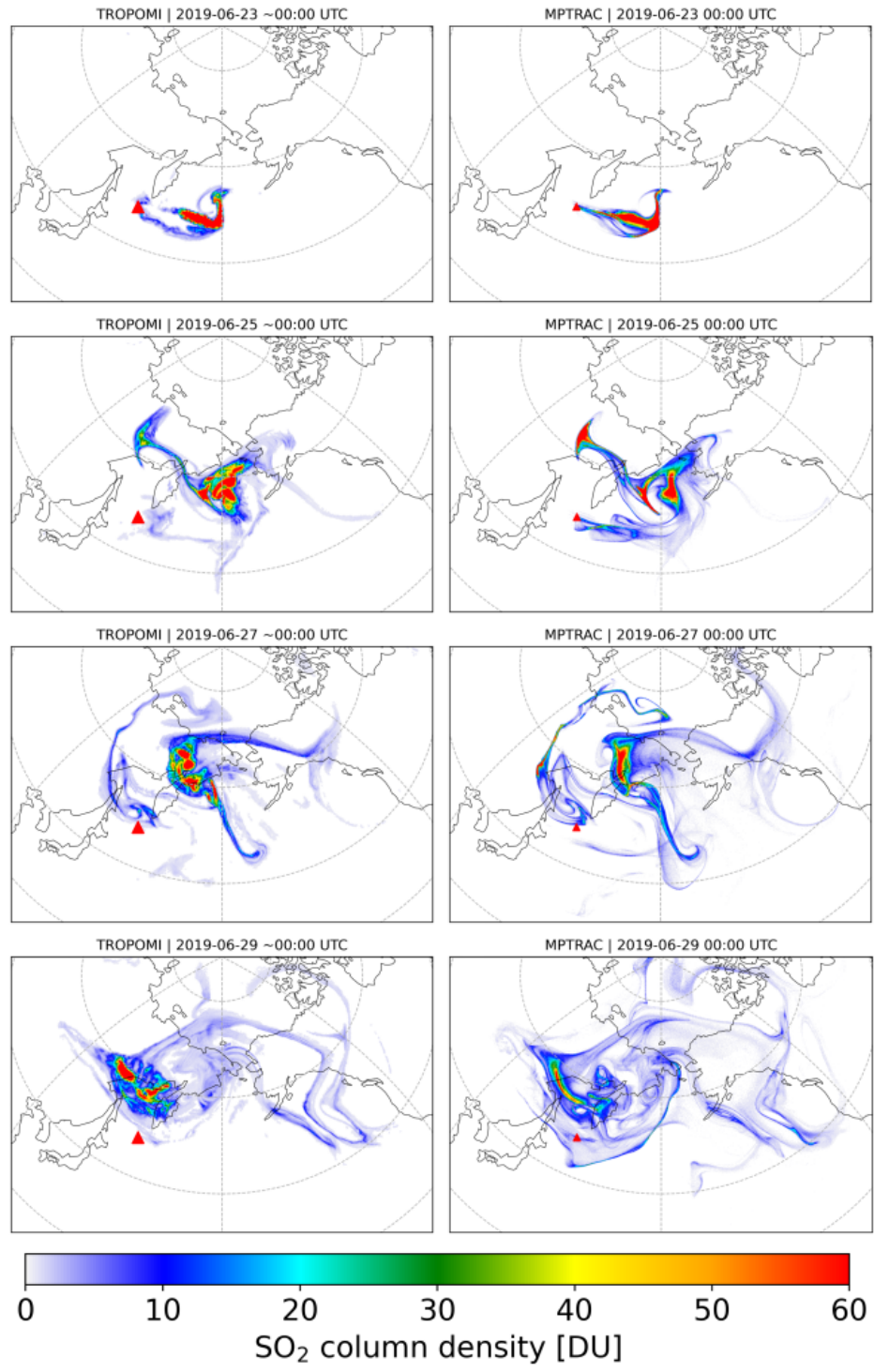
Figure 3. Evolution of SO₂ total column density distributions from 23 June 2019 to ~~30~~ 29 June 2019 from the MPTRAC simulation with implicit chemistry scheme (right column) and TROPOMI satellite observations (left column). The red triangle marks the location of the Raikoke volcano.
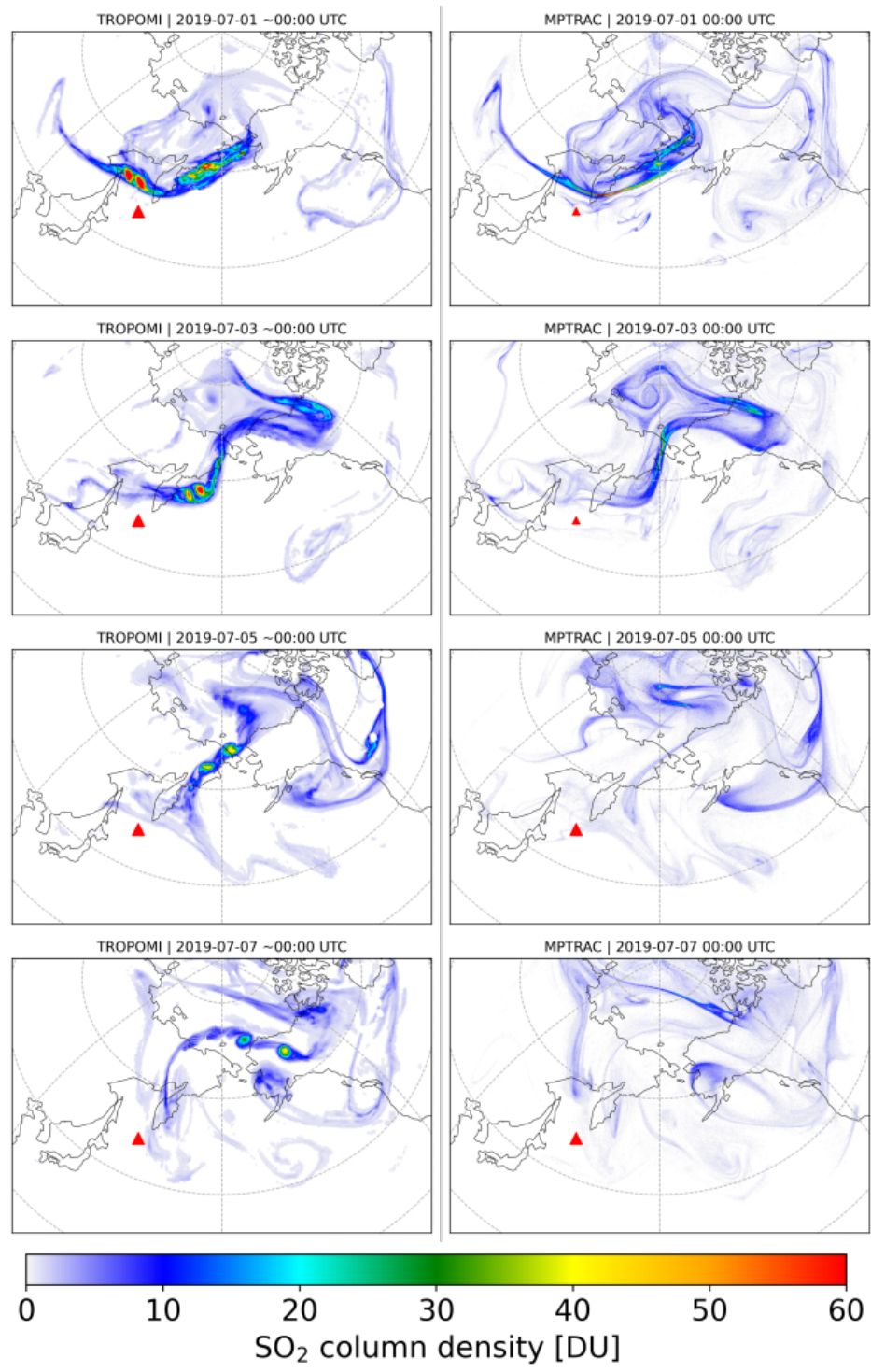
Figure 4. Same as Fig. 3, but from 1 July 2019 to 7 July 2019.
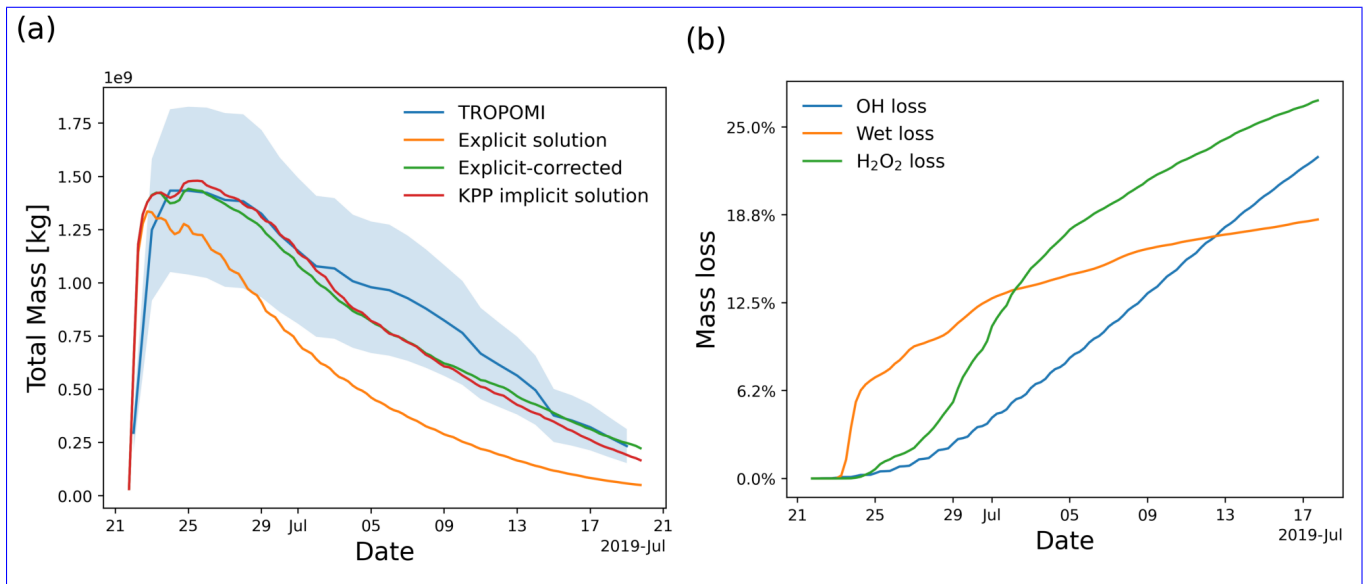
Figure 5. (a) Temporal evolution of the SO$_2$ total mass burden of the 2019 Raikoke eruption from TROPOMI measurements (blue curve, shading shows uncertainty range) and MPTRAC simulations with explicit solution (orange curve), simplified explicit solution with correction (green curve), and KPP implicit solution (red curve). (b) Estimates of SO$_2$ total mass loss of the Raikoke eruption due to OH oxidation (blue curve), wet deposition (orange curve), and H$_2$O$_2$ oxidation (green curve) from the simplified explicit solution with correction.

output of the model ~~was~~ were sampled with a lower detection limit of 0.35 DU and weighted by the mean kernel function of the TROPOMI observations to reduce the impact of noise and other uncertainties and to account for the vertical sensitivity of

270 the measurements. ~~The~~ It is found that the SO$_2$ lifetime modeled with the implicit KPP solution is about 1.6 times ~~longer~~ larger than that of the simplified explicit approximation. This can also be seen from ~~the vertical profile~~ a comparison of the vertical profiles of the e-folding ~~lifetime~~ lifetimes in Fig. 6.

The lifetime profile obtained with the KPP implicit solution indicates that the SO$_2$ has much longer lifetimes at higher altitudes. The lifetime is typically within a few hours to several days below 5 km of altitude, while it exceeds 10 to 100 days

275 above 5 km of altitude. Due to the frequent presence of clouds in the lower and middle troposphere, SO$_2$ is taken up into the liquid phase and decays rapidly due to cloud phase oxidation with H$_2$O$_2$ and wet deposition, leading to the shorter lifetime compared with the stratosphere. The vertical lifetime profile of the implicit KPP scheme shows a peak in the stratosphere that is not found in the explicit scheme. This is attributed to a reduction of the OH concentration within the SO$_2$ plume, which is captured by the implicit chemistry scheme but not by the explicit scheme, which uses a constant OH climatology.

280 ~~Temporal evolution of the SO$_2$ total mass burden of the 2019 Raikoke eruption from TROPOMI measurements (blue curve, shading shows uncertainty range) and MPTRAC simulations with explicit solution (orange curve), simplified explicit solution with correction (green curve), and KPP implicit solution (red curve).~~
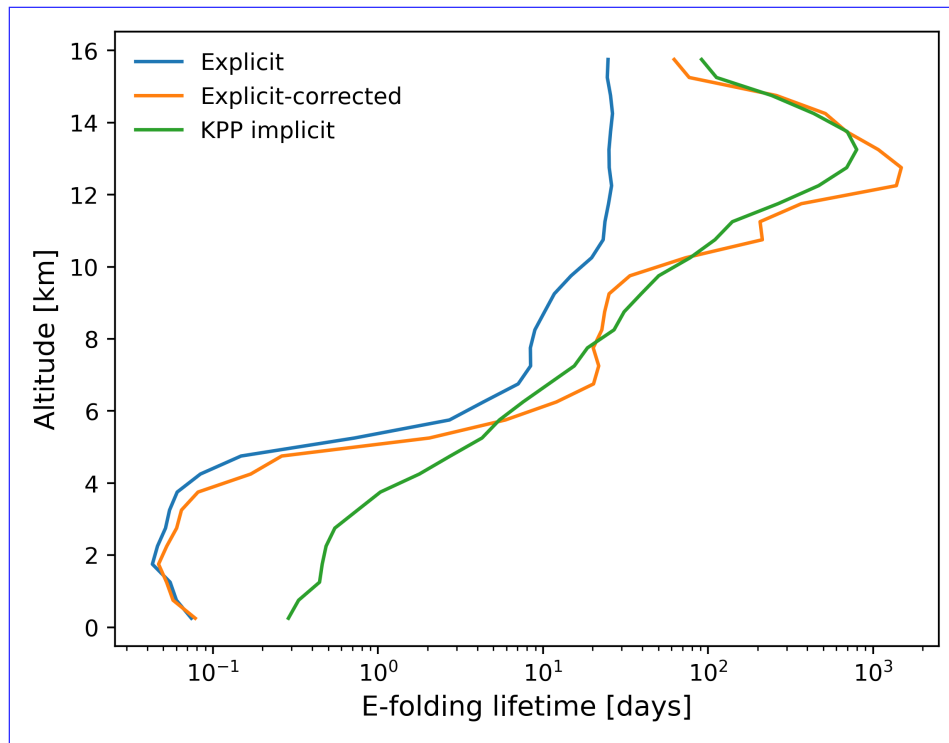
Figure 6. Vertical profiles of the average SO_2 e-folding lifetime of MPTRAC simulations with explicit solution (green curve), explicit solution with correction (orange curve) and KPP implicit solution (blue curve) during 25 June to 4 July.

 While still within the uncertainty range of the TROPOMI observations, Fig. 5a highlights a notable discrepancy between the SO_2 total mass from TROPOMI and the MPTRAC simulations during 3–15 July 2019. de Leeuw et al. (2021) attributed the change in SO_2 lifetime observed by TROPOMI about 10 days after the eruption to the removal of a large fraction of the tropospheric SO_2 mass through aqueous phase oxidation and wet deposition. Beyond this point, the TROPOMI observations become dominated by the stratospheric component of the SO_2 cloud. Since the stratosphere contains much less moisture, SO_2 removal occurs at a much lower rate, primarily through gas phase reactions with OH, leading to significantly longer e-folding lifetimes. Our MPTRAC simulations are based on the SO_2 injection profiles provided by Cai et al. (2022), which may underestimate the stratospheric fraction and, consequently, the impact on long-range transport. However, the estimates of SO_2 mass loss from the MPTRAC simulations (Fig. 5b) indicate a significant reduction in loss rates from wet deposition and H_2O_2 oxidation after July 3. This aligns closely with the findings of de Leeuw et al. (2021).

3.3   Correction for the simplified explicit scheme

From Figs. 5 and 6, it can be seen that the simplified explicit approximation overestimates the SO_2 decay rate by $\sim 60\%$ compared to the TROPOMI observations, whereas the implicit KPP solution agrees well with the TROPOMI observations. Hence, there is also a $\sim 60\%$ difference between the explicit and ~~the~~ KPP solution. This overestimation in the explicit scheme is likely due to changes in OH and other radicals resulting from the SO_2 injection itself, which are not accounted for in the climatology. To account for that, we ~~perform a SO_2dependent~~ developed an SO_2-dependent correction to the OH climatology. Essentially, the simplification of the explicit scheme applies a linear approximation to describe the non-linear oxidation processes. To compare the differences in lifetime of the two schemes, we performed another simulation without SO_2 injections to estimate the undisturbed background levels of OH and H_2O_2 and ~~compare~~ compared them with the ~~situation conditions~~ in the SO_2 ~~plumes~~plume. Figure 7 shows the ratio of the OH and H_2O_2 concentrations in the SO_2 plume versus the background oxidant concentrations as a function of SO_2 VMR. The ratio decreases as the abundance of SO_2 increases, which means that the depletion of the oxidants is faster than their production. In highly-concentrated SO_2 regions the oxidants are almost completely depleted.

Note that the data points shown in Fig. 7 are filtered using a Z-score threshold, because there are factors other than the chemical reactions that will affect the SO_2 distributions such as diffusion, convection, wet deposition, etc., causing the data not to be statistically ~~reliable~~representative. After filtering outliers with low Z-scores, a correction formula to estimate OH concentrations in the plume from OH background levels and the SO_2 concentration can be obtained by regression,

$$[OH] = 4.72 \times 10^{-8} [SO_2]^{-0.83} \times [OH]_{background}. \tag{3}$$

Similarly, the correction formula for H_2O_2 is

$$[H_2O_2] = 3.13 \times 10^{-6} [SO_2]^{-0.57} \times [H_2O_2]_{background}. \tag{4}$$

By applying the corrections to the climatological OH and H_2O_2 data to account for their removal in the SO_2 plume, a simulation with the simplified explicit approximation with correction can be conducted. Figure 6 shows that above $10\,km$ of altitude, the correction for the simplified explicit solution shifts the simulated lifetime closer to the KPP implicit solution. The correction reduces the amount of the oxidants when SO_2 is highly abundant in the volcanic plume. The mass evolution simulated by the corrected explicit solution is therefore in better agreement with the TROPOMI measurements and the KPP implicit solution (Fig. 5). These results reflect the fact that the chemical degradation of volcanic SO_2 is a non-linear process, which means that it should not simply be treated as a pseudo-first-order reaction. The correction of the OH and H_2O_2 concentrations applied to the explicit solution improves the representation of SO_2 decay in the ~~transport~~ chemistry-transport simulations, with almost no additional computational overhead.

3.4   Evaluation of the simulated OH field

The hydroxyl radical (OH) is an important oxidant in atmospheric chemistry, controlling the chemical decomposition of various species. For chemistry-transport simulations of volcanic SO_2 in the UT/LS region, oxidation via OH is the main factor of mass
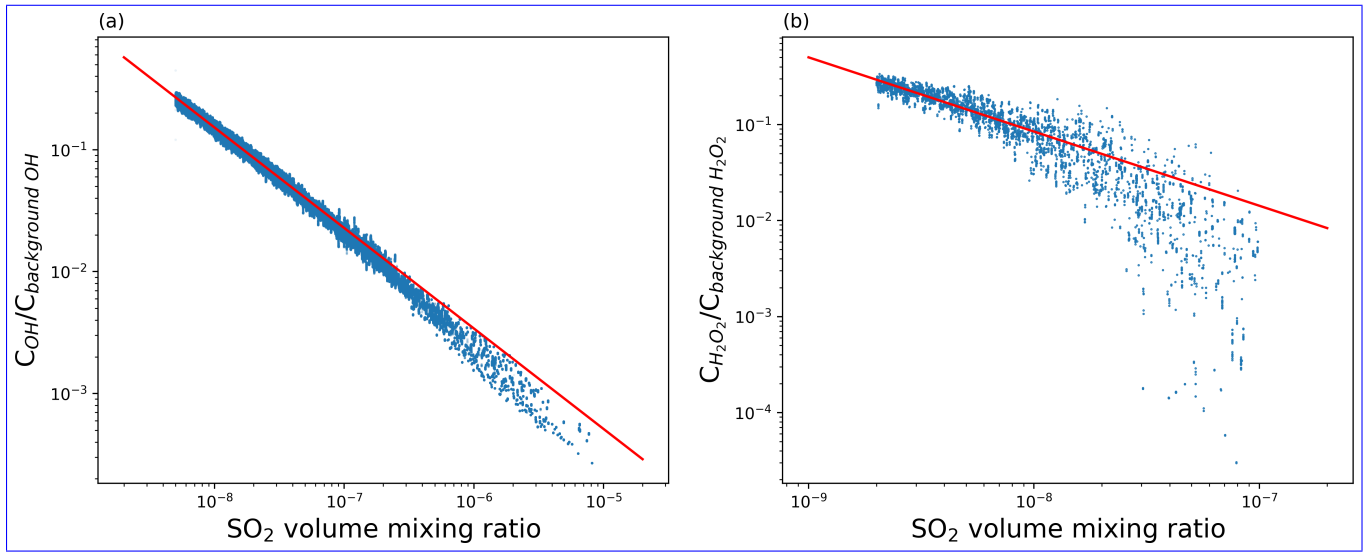
Figure 7. Ratio of OH concentration in dry atmosphere (a) and H_2O_2 concentration in cloud regions (b) in the Raikoke SO_2 plume versus background levels as a function of the SO_2 VMR. Each data point represents a single air parcel. The red ~~curves~~ lines represent the regression formulas given in Eqs. (3) and (4).

decay in the gas phase. In order to simulate the OH background conditions during the Raikoke case study without any enhanced levels of volcanic SO_2 abundance with the chemical mechanism introduced in Sect. 2.2.2, we distributed a total of 1 million air parcels in between 9 to 17 km of altitude. The fourth generation Copernicus Atmosphere Monitoring Service (CAMS) global

330 reanalysis data (Inness et al., 2019) were then used to compare with the OH field obtained with the implicit chemistry scheme implemented in MPTRAC. The CAMS reanalysis combines model data with observations using data assimilation techniques, providing a global distribution of atmospheric species. Key species assimilated in the CAMS reanalysis include ozone (O_3), carbon monoxide (CO), nitrogen dioxide (NO_2), methane (CH_4), and carbon dioxide (CO_2). Note that the hydroxyl radical (OH) and hydrogen peroxide (H_2O_2) are not directly assimilated from observations; instead, their concentrations are computed

335 using the chemistry scheme implemented in the CAMS reanalysis.

Figure 8 ~~shows a comparison of OH zonal mean~~ compares zonal mean OH distributions at different pressure levels from ~~CAMS, MPTRAC~~the CAMS reanalysis, the MPTRAC model, and the CLaMS ~~zonal mean climatologyPommrich et al. (2014). Both the CAMS reanalysis data and the CLaMS climatological datahave been evaluated by comparison with in-situ measurements in Liu et al. (2023). Furthermore, Fig.~~ climatology. The best agreement among the three datasets is observed at the 100 hPa

340 pressure level. Zonal mean OH concentrations increase gradually from near zero under polar winter conditions at high southern latitudes to approximately 2.5×10^{-13} ppv in the northern subtropics. At northern mid and high latitudes, OH concentrations remain within 1.5 to 2×10^{-13} ppv. At lower vertical levels (150 to 250 hPa), differences of up to a factor of two are observed in the tropics and at northern mid- to high latitudes. Overall, the CAMS and MPTRAC datasets tend to agree more closely with each other than with the CLaMS data. Differences in OH concentrations arise from variations in chemical mechanisms,
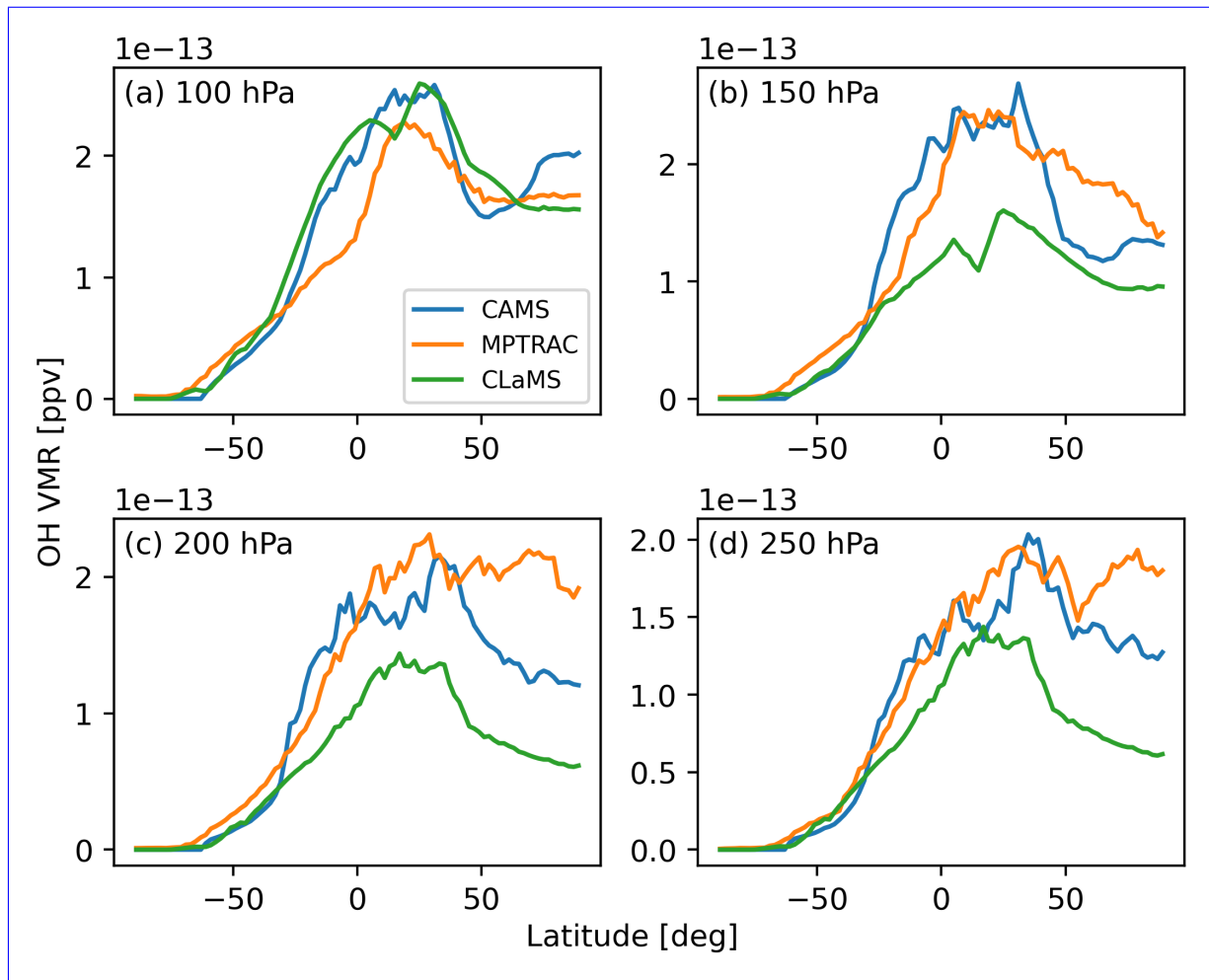
Figure 8. Zonal mean distributions of the OH field obtained from the CAMS reanalysis (blue curves), climatological data from the CLaMS model (green curves) and the MPTRAC simulation (orange curves) at pressure levels of 100 hPa (a), 150 hPa (b), 200 hPa (c) and 250 hPa (d) on 1 July 2019, 00:00 UTC.

345   emissions, meteorological conditions, photolysis schemes, spatial resolution, boundary conditions, and the representation of stratosphere-troposphere exchange processes.

Figure 9 shows the global CAMS and MPTRAC OH fields at pressure levels of ~ 100 hPa, ~ 150 hPa, ~ 200 hPa and ~ 250 100 to 250 hPa on 1 July 2019, 00:00 UTC. The OH fields obtained by MPTRAC show some similar were generated using its implicit chemistry scheme under SO_2-free conditions. The MPTRAC OH fields exhibit similar spatial distributions

350   with respect to the solar zenith angle dependence as CAMS, which is due to the CAMS data, reflecting the strong correlation between OH production and solar radiation. The OH fields simulated by the different models are at the same magnitude.

~~The MPTRAC chemistry modeling can~~ magnitudes of the OH concentrations produced by the two models are comparable, underscoring the reliability of MPTRAC in capturing key OH dynamics.

A closer inspection reveals distinct features in the CAMS OH fields that are absent in the MPTRAC fields, such as localized OH plumes over Japan and the Pacific visible in the CAMS data. This discrepancy likely stems from the simplified oxidant mechanisms used in MPTRAC, which smooth out regional OH enhancements captured by CAMS. Additional factors, such as differences in spatial and temporal resolution and the representation of regional emissions and environmental conditions, further contribute to the observed differences. Despite these limitations, the MPTRAC scheme demonstrates a reasonable ability to simulate the production and loss of the short-lived OH radical in the UT/LS region~~at reasonable accuracy, which is essential for SO2 lifetime modeling~~, offering a practical balance between accuracy and computational efficiency for modeling SO_2 lifetimes in volcanic plumes and other atmospheric scenarios.

3.5 Selection of the chemistry time step

In MPTRAC, a fixed time step is applied for numerical integration of the trajectories and in most other modules. Based on previous studies (Rößler et al., 2018; Clemens et al., 2024), a time step of 180 s was selected for calculating trajectories with the midpoint method and considering the spatiotemporal resolution of the ERA5 reanalysis data. This choice of the time step provides a reasonable trade-off in terms of accuracy and computational costs of the trajectory calculations, i.e., it is small enough to consider integration errors negligible while providing a minimum in computation time. In terms of computation effort, the time step of 180 s is acceptable for the explicit solution, but it is not efficient for the implicit chemistry calculations, which is particularly demanding in terms of computation.

To improve the computational efficiency for the implicit chemistry scheme, we implemented a distinct time step for the chemistry calculations. The chemistry time step is an important control parameter, as it has a significant impact on the computational efficiency. The chemistry time step size should be as large as possible without compromising the accuracy of the results. Figure 10 shows the SO_2 total mass time evolution obtained by different chemistry time steps. The results diverge when the time step of ~~chemistry solution~~ the chemistry calculations is larger than 6 h. Therefore, we recommend using a chemistry time step of 3 to 6 h to balance the computational efficiency and accuracy of the solution for the volcanic SO_2 oxidation.

3.6 Assessment of computational costs

The KPP-based implicit chemistry solver implemented in MPTRAC can solve complex chemical mechanisms with flexible definition of the chemical reactions and species. In the case of the volcanic SO_2 chemistry-transport simulations, the corrected explicit solution achieves similar results with higher computational efficiency. For now, GPU offloading has been implemented using OpenACC for the simplified explicit scheme, while for the implicit scheme this is planned for the future. Figure 11 shows the runtime of MPTRAC simulations on the JUWELS supercomputer at the Jülich Supercomputing Centre comparing the implicit and explicit chemistry schemes using a chemistry time step of 21600 s and 180 s, respectively. The CPU simulations were conducted on a single compute node of the JUWELS Cluster (Jülich Supercomputing Centre, 2019), parallelized with 48
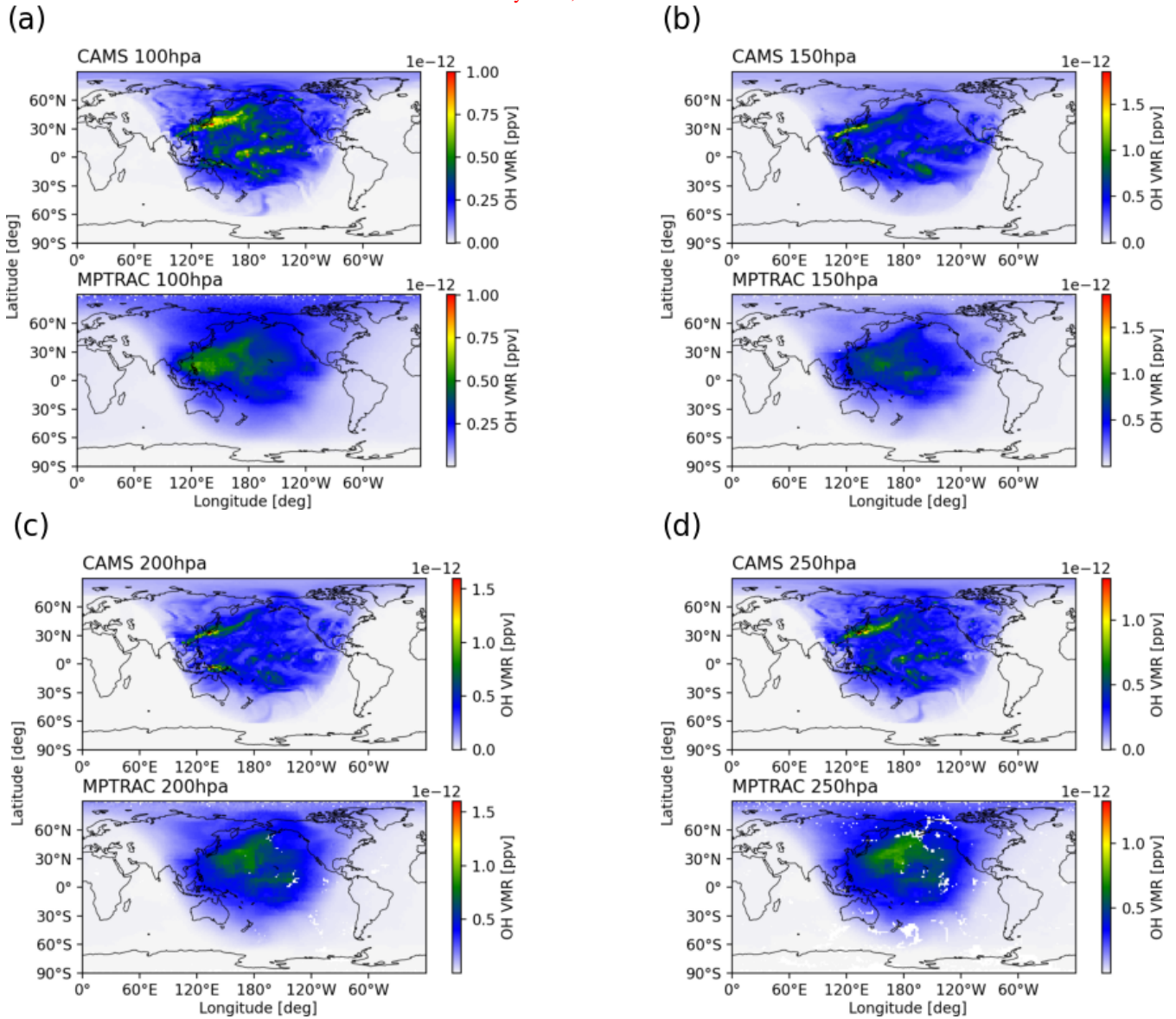
Figure 9. Global OH fields obtained from the CAMS reanalysis (top) and MPTRAC simulations (bottom) at pressure levels of 100 hPa (a), 150 hPa (b), 200 hPa (c) and 250 hPa (d) on 1 July 2019, 00:00 UTC.
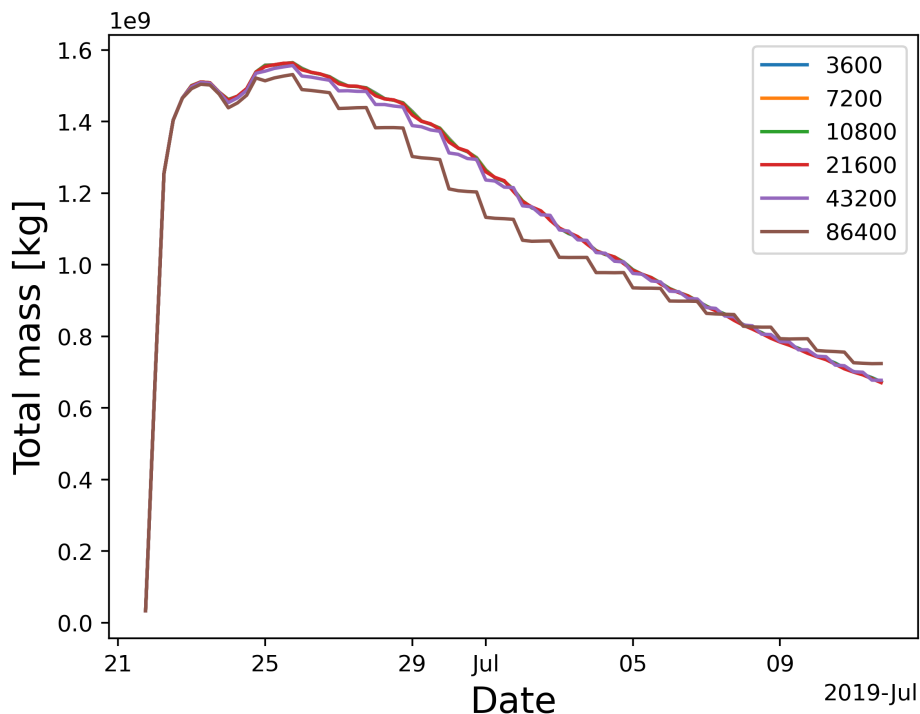
Figure 10. Total mass burden evolution simulated with different chemistry time step size settings of 3600, 7200, 10800, 21600, 43200 and 86400 seconds (see plot key).

385 OpenMP threads. Each compute node of JUWELS Cluster contains 2 Intel Xeon Platinum 8168 CPUs with 24 physical cores per CPU. The GPU simulations were conducted on JUWELS Booster (Jülich Supercomputing Centre, 2021) with 2 AMD EPYC Rome 7402 CPUs and 4 NVIDIA A100 GPUs per node.

Regarding the chemistry, ~~Figure~~ Fig. 11a shows that the simplified explicit solution is about 5.3 times faster than the KPP implicit solution for a simulation with 1 million air parcels. Considering that file-I/O and meteorological data preprocessing

390 also require a substantial part of the total runtime, the total runtime is reduced by $\sim 56\%$ by choosing the more efficient explicit chemistry scheme. The GPU solution of the simplified explicit chemistry scheme on JUWELS Booster reduces the total runtime by $\sim 75\%$, with the runtime required for chemistry becoming nearly negligible. As the scale of the simulation increases (i. e., for simulations with more air parcels), the advantage of the explicit solution in terms of computational efficiency becomes even more pronounced. Figure 11b shows that the total runtime is reduced by 92% for a simulation with 3 million air parcels. This

395 improvement in computational efficiency is particularly relevant for large-scale chemistry transport simulations, where finding the proper trade-off between accuracy and computational costs is most critical. In the future, the KPP implicit scheme might also be equipped with GPU offloading to improve its performance (Alvanos and Christoudias, 2017; Christoudias et al., 2021).
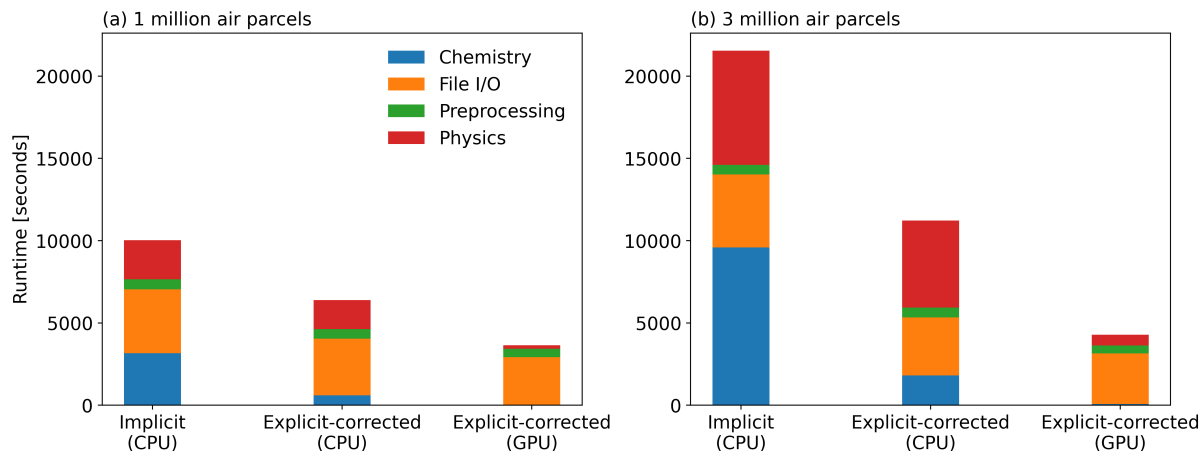
Figure 11. Computational costs of the Raikoke simulations with different chemistry schemes (the implicit scheme and the simplified explicit scheme with correction) on the JUWELS Cluster (CPU) and JUWELS Booster (GPU) for a simulation with 1 million air parcels on a scale of 1 million air parcels (a) and 3 million air parcels (b). The blue bar represents the runtime for the chemistry calculations, while the red bar represents the runtime for the other physical modules besides chemistry.

4   Summary and conclusions

The Lagrangian transport model MPTRAC ~~provides two alternative schemes to simulate SO₂ chemistry for volcanic eruptions.~~ ~~The explicit scheme uses monthly mean zonal climatology data of radical species to determine~~ offers two schemes for simulating SO₂ chemistry in volcanic eruptions: an explicit approach utilizing climatological data for reaction rates and ~~calculate mass loss as an exponential decay of SO₂ . The implicit scheme uses the Rosenbrock integrator provided by the~~ ~~KPP software package to calculate the~~ SO₂ decay, and an implicit approach leveraging KPP's Rosenbrock integrator for multi-species chemical ~~reaction~~ processes. KPP can solve complex chemical mechanisms with flexible definition of chemical species, reactions, and rate coefficients. The implicit solution allows for more complex, non-linear chemical ~~mechanisms~~ mechanisms with dynamic reaction rates depending on the species concentrations. Here, we propose a chemical mechanism with 31 reactions and 12 species to model the production and loss of the short-lived OH radical and H_2O_2, which are essential for the decomposition of SO_2 in the gas and aqueous phase, respectively, in the UT/LS region. The mechanism proposed here can serve as a basis for developing more complex chemical mechanisms in future studies. It could also be further optimized by evaluating the relevance of each reaction pathway to reduce the computational effort.

The OH radical is the main oxidant in the gas phase, which largely controls the decomposition of SO_2 in the UT/LS. We compared ~~the OH radical field~~ OH radical fields obtained by the proposed mechanism in MPTRAC with CAMS reanalysis data and climatological data from the CLaMS model. The OH radical field obtained by the proposed mechanism shows a clear characteristic of diurnal variation and concentrations at a similar level compared to these reference data sets. The cloud phase H_2O_2 oxidation also has a significant impact on the SO_2 decay in the lower troposphere. It must be taken into account to

properly represent the loss of tropospheric SO_2 over time, especially for other volcanic eruptions, such as those happening in the tropics with lower peak emission heights (Liu et al., 2023). Cloud phase oxidation has been considered in all cases in this study.

Applying the chemical mechanisms to the June 2019 Raikoke eruption, the implicit KPP-based solution aligns well with TROPOMI satellite data on SO_2 mass burden evolution, while the simplified explicit approach overestimates SO_2 decay by 60%. This overestimation is due to using OH and H_2O_2 climatological background field without considering enhanced levels of SO_2. Regression-derived correction formulas for OH and H_2O_2 concentrations ($y = ax^b$) adjust climatology-based oxidant levels, introducing non-linear effects that enhance SO_2 lifetime representation in explicit simulations. We also applied the correction to another volcanic eruption, the July 2018 Ambae eruption (Liu et al., 2023), and observed that it produced a total SO_2 lifetime comparable to that predicted by the KPP implicit solution. Notably, despite differences in geographic and atmospheric condition – Ambae being a tropical eruption and Raikoke occurring in Northern Hemisphere mid- and high latitudes – the same parameter values for a and b in the correction formula were used. This suggests that the correction approach is transferable across diverse eruption scenarios.

The corrected explicit solution achieves realistic lifetime modeling with more than five times the efficiency of the implicit approach, making it ideal for computationally demanding applications such as emission reconstruction through inverse modeling. Previous studies using backward trajectory methods for volcanic SO_2 lacked realistic chemical lifetime modeling, a limitation now being addressed. Ongoing development includes inverse modeling techniques for source estimation, incorporating support for nonlinear chemical mechanisms and investigating the interplay between lifetime modeling and source reconstruction. These advancements significantly enhance MPTRAC's Lagrangian chemistry modeling

450 ~~and applications~~ capabilities, enabling more precise source estimation and positioning the model for broader applications on modern HPC systems.

. The MPTRAC model (Hoffmann et al., 2016, 2022) is distributed under the terms and conditions of the GNU General Public License (GPL) version 3. The version 2.7 release of MPTRAC used in this paper is archived on Zenodo (Hoffmann et al., 2024a). Newer versions of MPTRAC are available from the repository at https://github.com/slcs-jsc/mptrac (last access: 3 December 2024). The ERA5 data were
455 obtained from the European Centre for Medium-Range Weather Forecasts, see https://www.ecmwf.int/en/forecasts/datasets (Hersbach et al., 2020). The TROPOMI data (Theys et al., 2017) are provided via the Copernicus Data Space Ecosystem.

. Conceptualization: M.L. and L.H.; Data curation: L.H., S.G., J.G. and Z.C.; Formal analysis: M.L.; Methodology: L.H., J.G. and Y.H.; Software: M.L. and L.H.; Supervision: L.H.; Validation: M.L.; Writing – original draft: M.L. and L.H.; Writing - review & editing: M.L., L.H., S.G., J.G., Z.C. and Y.H.

460 . Jens-Uwe Grooß is a member of the editorial board of Atmospheric Chemistry and Physics.

. This research was supported by the Helmholtz Association of German Research Centres (HGF) through the Joint Laboratory for Exascale Earth System Modeling (JL-ExaESM). The authors are grateful to the Jülich Supercomputing Center for providing computing time and storage resources on the JUWELS supercomputer. We acknowledge the use of the AI tool DeepL for language editing.

References

Alvanos, M. and Christoudias, T.: GPU-accelerated atmospheric chemical kinetics in the ECHAM/MESSy (EMAC) Earth system model (version 2.52), Geosci. Model Dev., 10, 3679–3693, https://doi.org/10.5194/gmd-10-3679-2017, 2017.

Becker, G., Grooß, J.-U., McKenna, D. S., and Müller, R.: Stratospheric photolysis frequencies: Impact of an improved numerical solution of the radiative transfer equation, J. Atmos. Chem., 37, 217–229, https://doi.org/10.1023/A:1006468926530, 2000.

Bergamaschi, P., Segers, A., Brunner, D., Haussaire, J.-M., Henne, S., Ramonet, M., Arnold, T., Biermann, T., Chen, H., Conil, S., Delmotte, M., Forster, G., Frumau, A., Kubistin, D., Lan, X., Leuenberger, M., Lindauer, M., Lopez, M., Manca, G., Müller-Williams, J., O'Doherty, S., Scheeren, B., Steinbacher, M., Trisolino, P., Vítková, G., and Yver Kwok, C.: High-resolution inverse modelling of European CH_4 emissions using the novel FLEXPART-COSMO TM5 4DVAR inverse modelling system, Atmos. Chem. Phys., 22, 13 243–13 268, https://doi.org/10.5194/acp-22-13243-2022, 2022.

Brunner, D.: Atmospheric Chemistry in Lagrangian Models—Overview, chap. 19, pp. 224–234, American Geophysical Union (AGU), https://doi.org/10.1029/2012GM001431, 2012.

Brunner, D., Arnold, T., Henne, S., Manning, A., Thompson, R. L., Maione, M., O'Doherty, S., and Reimann, S.: Comparison of four inverse modelling systems applied to the estimation of HFC-125, HFC-134a, and SF_6 emissions over Europe, Atmos. Chem. Phys., 17, 10 651–10 674, https://doi.org/10.5194/acp-17-10651-2017, 2017.

Burkholder, J. B., Sander, S. P., J. Abbatt, J. R. B., Cappa, C., Crounse, J. D., Dibble, T. S., Huie, R. E., Kolb, C. E., Kurylo, M. J., Orkin, V. L., Percival, C. J., Wilmouth, D. M., and Wine, P. H.: Chemical kinetics and photochemical data for use in atmospheric studies: evaluation number 19, Tech. rep., Jet Propulsion Laboratory, Pasadena, 2019.

Cai, Z., Griessbach, S., and Hoffmann, L.: Improved estimation of volcanic SO_2 injections from satellite retrievals and Lagrangian transport simulations: the 2019 Raikoke eruption, Atmos. Chem. Phys., 22, 6787–6809, https://doi.org/10.5194/acp-22-6787-2022, 2022.

Che, K., Cai, Z., Liu, Y., Wu, L., Yang, D., Chen, Y., Meng, X., Zhou, M., Wang, J., Yao, L., and Wang, P.: Lagrangian inversion of anthropogenic CO2 emissions from Beijing using differential column measurements, Environ. Res. Lett., 17, 075 001, https://doi.org/10.1088/1748-9326/ac7477, 2022.

Christoudias, T., Kirfel, T., Kerkweg, A., Taraborrelli, D., Moulard, G.-E., Raffin, E., Azizi, V., Oord, G. v. d., and Werkhoven, B. v.: GPU Optimizations for Atmospheric Chemical Kinetics, in: The International Conference on High Performance Computing in Asia-Pacific Region, HPCAsia '21, p. 136–138, Association for Computing Machinery, New York, NY, USA, https://doi.org/10.1145/3432261.3439863, 2021.

Clemens, J., Hoffmann, L., Vogel, B., Grießbach, S., and Thomas, N.: Implementation and evaluation of diabatic advection in the Lagrangian transport model MPTRAC 2.6, Geosci. Model Dev., 17, 4467–4493, https://doi.org/10.5194/gmd-17-4467-2024, 2024.

Collins, W., Johnson, C., and Derwent, R.: Tropospheric Ozone in a Global-Scale Three-Dimensional Lagrangian Model and Its Response to NO X Emission Controls, J. Atmos. Chem., 26, 223–274, https://doi.org/10.1023/A:1005836531979, 1997.

Dalsøren, S. B., Myhre, G., Hodnebrog, Ø., Myhre, C. L., Stohl, A., Pisso, I., Schwietzke, S., Höglund-Isaksson, L., Helmig, D., Reimann, S., et al.: Discrepancy between simulated and observed ethane and propane levels explained by underestimated fossil emissions, Nat. Geosci., 11, 178–184, https://doi.org/https://doi.org/10.1038/s41561-018-0073-0, 2018.

Damian, V., Sandu, A., Damian, M., Potra, F., and Carmichael, G. R.: The kinetic preprocessor KPP-a software environment for solving chemical kinetics, Comput. Chem. Eng., 26, 1567–1579, https://doi.org/10.1016/S0098-1354(02)00128-X, 2002.

500   de Leeuw, J., Schmidt, A., Witham, C. S., Theys, N., Taylor, I. A., Grainger, R. G., Pope, R. J., Haywood, J., Osborne, M., and Kristiansen, N. I.: The 2019 Raikoke volcanic eruption – Part 1: Dispersion model simulations and satellite retrievals of volcanic sulfur dioxide, Atmos. Chem. Phys., 21, 10 851–10 879, https://doi.org/10.5194/acp-21-10851-2021, 2021.

Dee, D. P., Uppala, S. M., Simmons, A. J., Berrisford, P., Poli, P., Kobayashi, S., Andrae, U., Balmaseda, M. A., Balsamo, G., Bauer, P., Bechtold, P., Beljaars, A. C. M., van de Berg, L., Bidlot, J., Bormann, N., Delsol, C., Dragani, R., Fuentes, M., Geer, A. J.,
505   Haimberger, L., Healy, S. B., Hersbach, H., Hólm, E. V., Isaksen, L., Kållberg, P., Köhler, M., Matricardi, M., McNally, A. P., Monge-Sanz, B. M., Morcrette, J.-J., Park, B.-K., Peubey, C., de Rosnay, P., Tavolato, C., Thépaut, J.-N., and Vitart, F.: The ERA-Interim reanalysis: configuration and performance of the data assimilation system, Quart. J. Roy. Meteorol. Soc., 137, 553–597, https://doi.org/10.1002/qj.828, 2011.

Evangeliou, N., Kylling, A., Eckhardt, S., Myroniuk, V., Stebel, K., Paugam, R., Zibtsev, S., and Stohl, A.: Open fires in Greenland
510   in summer 2017: transport, deposition and radiative effects of BC, OC and BrC emissions, Atmos. Chem. Phys., 19, 1393–1411, https://doi.org/10.5194/acp-19-1393-2019, 2019.

Gerbig, C., Lin, J. C., Wofsy, S. C., Daube, B. C., Andrews, A. E., Stephens, B. B., Bakwin, P. S., and Grainger, C. A.: Toward constraining regional-scale fluxes of CO2 with atmospheric observations over a continent: 2. Analysis of COBRA data using a receptor-oriented framework, J. Geophys. Res., 108, 4757, https://doi.org/10.1029/2003JD003770, 2003.

515   Gorkavyi, N., Krotkov, N. A., Li, C., Lait, L. R., Colarco, P. R., Carn, S. A., DeLand, M. T., Newman, P. A., Schoeberl, M. R., Taha, G., Torres, O., Vasilkov, A. P., and Joiner, J.: Tracking Aerosols and SO_2 Clouds From the Raikoke Eruption: 3D View From Satellite Observations, Atmos. Meas. Tech., https://doi.org/10.5194/amt-14-7545-2021, 2021.

Heng, Y., Hoffmann, L., Griessbach, S., Roessler, T., and Stein, O.: Inverse transport modeling of volcanic sulfur dioxide emissions using large-scale simulations, Geosci. Model Dev., 9, 1627–1645, https://doi.org/10.5194/gmd-9-1627-2016, 2016.

520   Henze, D. K., Hakami, A., and Seinfeld, J. H.: Development of the adjoint of GEOS-Chem, Atmos. Chem. Phys., 7, 2413–2433, https://doi.org/10.5194/acp-7-2413-2007, 2007.

Hersbach, H., Bell, B., Berrisford, P., Hirahara, S., Horanyi, A., Munoz-Sabater, J., Nicolas, J., Peubey, C., Radu, R., Schepers, D., Simmons, A., Soci, C., Abdalla, S., Abellan, X., Balsamo, G., Bechtold, P., Biavati, G., Bidlot, J., Bonavita, M., De Chiara, G., Dahlgren, P., Dee, D., Diamantakis, M., Dragani, R., Flemming, J., Forbes, R., Fuentes, M., Geer, A., Haimberger, L., Healy, S., Hogan, R. J., Holm, E.,
525   Janiskova, M., Keeley, S., Laloyaux, P., Lopez, P., Lupu, C., Radnoti, G., de Rosnay, P., Rozum, I., Vamborg, F., Villaume, S., and Thepaut, J.-N.: The ERA5 global reanalysis, Quart. J. Roy. Meteorol. Soc., 146, 1999–2049, https://doi.org/10.1002/qj.3803, 2020.

Hoffmann, L., Baumeister, P. F., Cai, Z., Clemens, J., Griessbach, S., Günther, G., Heng, Y., Liu, M., Haghighi Mood, K., Stein, O., Thomas, N., Vogel, B., Wu, X., and Zou, L.: Massive-Parallel Trajectory Calculations version 2.2 (MPTRAC-2.2): Lagrangian transport simulations on graphics processing units (GPUs), Geosci. Model Dev., 15, 2731–2762, https://doi.org/10.5194/gmd-15-2731-2022, 2022.

530   Hoffmann, L., Konopka, P., Clemens, J., and Vogel, B.: Lagrangian transport simulations using the extreme convection parameterization: an assessment for the ECMWF reanalyses, Atmos. Chem. Phys., 23, 7589–7609, https://doi.org/10.5194/acp-23-7589-2023, 2023.

Hoffmann, L., Clemens, J., Griessbach, S., Haghighi Mood, K., Khosrawi, F., Liu, M., Lu, Y.-S., Sonnabend, J., and Zou, L.: Massive-Parallel Trajectory Calculations (MPTRAC) v2.7, https://doi.org/10.5281/zenodo.12751121, 2024a.

Hoffmann, L., Haghighi Mood, K., Herten, A., Hrywniak, M., Kraus, J., Clemens, J., and Liu, M.: Accelerating Lagrangian transport
535   simulations on graphics processing units: performance optimizations of Massive-Parallel Trajectory Calculations (MPTRAC) v2.6, Geosci. Model Dev., 17, 4077–4094, https://doi.org/10.5194/gmd-17-4077-2024, 2024b.

Hoffmann, L., Roessler, T., Griessbach, S., Heng, Y., and Stein, O.: Lagrangian transport simulations of volcanic sulfur dioxide emissions: Impact of meteorological data products, J. Geophys. Res., 121, 4651–4673, https://doi.org/10.1002/2015JD023749, 2016.

Hoffmann, L., Guenther, G., Li, D., Stein, O., Wu, X., Griessbach, S., Heng, Y., Konopka, P., Mueller, R., Vogel, B., and Wright, J. S.: From ERA-Interim to ERA5: the considerable impact of ECMWF's next-generation reanalysis on Lagrangian transport simulations, Atmos. Chem. Phys., 19, 3097–3124, https://doi.org/10.5194/acp-19-3097-2019, 2019.

Hoppe, C. M., Hoffmann, L., Konopka, P., Grooß, J.-U., Ploeger, F., Günther, G., Jöckel, P., and Müller, R.: The implementation of the CLaMS Lagrangian transport core into the chemistry climate model EMAC 2.40.1: application on age of air and transport of long-lived trace species, Geosci. Model Dev., 7, 2639–2651, https://doi.org/10.5194/gmd-7-2639-2014, 2014.

Inness, A., Ades, M., Agusti-Panareda, A., Barre, J., Benedictow, A., Blechschmidt, A.-M., Dominguez, J. J., Engelen, R., Eskes, H., Flemming, J., Huijnen, V., Jones, L., Kipling, Z., Massart, S., Parrington, M., Pench, V.-H., Razinger, M., Remy, S., Schulz, M., and Suttie, M.: The CAMS reanalysis of atmospheric composition, Atmos. Chem. Phys., 19, 3515–3556, https://doi.org/10.5194/acp-19-3515-2019, 2019.

Jülich Supercomputing Centre: JUWELS: Modular Tier-0/1 Supercomputer at the Jülich Supercomputing Centre, J. Large-scale Res. Facilities, 5, A135, https://doi.org/10.17815/jlsrf-5-171, 2019.

Jülich Supercomputing Centre: JUWELS Cluster and Booster: Exascale Pathfinder with Modular Supercomputing Architecture at Jülich Supercomputing Centre, J. Large-scale Res. Facilities, 7, A183, https://doi.org/10.17815/jlsrf-7-183, 2021.

Kloss, C., Berthet, G., Sellitto, P., Ploeger, F., Taha, G., Tidiga, M., Eremenko, M., Bossolasco, A., Jégou, F., Renard, J., and Legras, B.: Stratospheric Aerosol Layer Perturbation Caused by the 2019 Raikoke and Ulawun Eruptions and Their Radiative Forcing, Atmos. Chem. Phys., https://doi.org/10.5194/acp-21-535-2021, 2021.

Lary, D. J. and Pyle, J. A.: Diffuse radiation, twilight, and photochemistry — I, J. Atmos. Chem., 13, 373–392, https://doi.org/10.1007/BF00057753, 1991.

Liu, M., Huang, Y., Hoffmann, L., Huang, C., Chen, P., and Heng, Y.: High-Resolution Source Estimation of Volcanic Sulfur Dioxide Emissions Using Large-Scale Transport Simulations, in: Computational Science – ICCS 2020, edited by Krzhizhanovskaya, V. V., Závodszky, G., Lees, M. H., Dongarra, J. J., Sloot, P. M. A., Brissos, S., and Teixeira, J., pp. 60–73, Springer International Publishing, https://doi.org/10.1007/978-3-030-50420-5_5, 2020.

Liu, M., Hoffmann, L., Griessbach, S., Cai, Z., Heng, Y., and Wu, X.: Improved representation of volcanic sulfur dioxide depletion in Lagrangian transport simulations: a case study with MPTRAC v2.4, Geosci. Model Dev., 16, 5197–5217, https://doi.org/10.5194/gmd-16-5197-2023, 2023.

McKenna, D. S., Grooß, J.-U., Günther, G., Konopka, P., Müller, R., Carver, G., and Sasano, Y.: A new Chemical Lagrangian Model of the Stratosphere (CLaMS) 2. Formulation of chemistry scheme and initialization, J. Geophys. Res., 107, ACH 4–1–ACH 4–14, https://doi.org/10.1029/2000JD000113, 2002a.

McKenna, D. S., Konopka, P., Grooß, J.-U., Günther, G., Müller, R., Spang, R., Offermann, D., and Orsolini, Y.: A new Chemical Lagrangian Model of the Stratosphere (CLaMS) 1. Formulation of advection and mixing, J. Geophys. Res., 107, ACH 15–1–ACH 15–15, https://doi.org/10.1029/2000JD000114, 2002b.

Minschwaner, K., Manney, G. L., Wang, S. H., and Harwood, R. S.: Hydroxyl in the stratosphere and mesosphere – Part 1: Diurnal variability, Atmos. Chem. Phys., 11, 955–962, https://doi.org/10.5194/acp-11-955-2011, 2011.

Pardini, F., Burton, M., de' Michieli Vitturi, M., Corradini, S., Salerno, G., Merucci, L., and Di Grazia, G.: Retrieval and intercomparison of volcanic SO2 injection height and eruption time from satellite maps and ground-based observations, J. Volcanol. Geotherm. Res., 331, 79–91, https://doi.org/10.1016/j.jvolgeores.2016.12.008, 2017.

Pattantyus, A. K., Businger, S., and Howell, S. G.: Review of sulfur dioxide to sulfate aerosol chemistry at Kilauea Volcano, Hawai'i, Atmos. Environment, 185, 262–271, https://doi.org/10.1016/j.atmosenv.2018.04.055, 2018.

Pommrich, R., Müller, R., Grooß, J.-U., Konopka, P., Ploeger, F., Vogel, B., Tao, M., Hoppe, C. M., Günther, G., Spelten, N., Hoffmann, L., Pumphrey, H.-C., Viciani, S., D'Amato, F., Volk, C. M., Hoor, P., Schlager, H., and Riese, M.: Tropical troposphere to stratosphere transport of carbon monoxide and long-lived trace species in the Chemical Lagrangian Model of the Stratosphere (CLaMS), Geosci. Model Dev., 7, 2895–2916, https://doi.org/10.5194/gmd-7-2895-2014, 2014.

Redington, A., Derwent, R., Witham, C., and Manning, A.: Sensitivity of modelled sulphate and nitrate aerosol to cloud, pH and ammonia emissions, Atmos. Environment, 43, 3227–3234, https://doi.org/10.1016/j.atmosenv.2009.03.041, 2009.

Rieger, V. S., Mertens, M., and Grewe, V.: An advanced method of contributing emissions to short-lived chemical species (OH and HO_2): the TAGGING 1.1 submodel based on the Modular Earth Submodel System (MESSy 2.53), Geosci. Model Dev., 11, 2049–2066, https://doi.org/10.5194/gmd-11-2049-2018, 2018.

Rolph, G., Draxler, R., and Depena, R.: Modeling Sulfur Concentrations and Depositions in the United-States During Anatex, Atmos. Environment, 26, 73–93, https://doi.org/10.1016/0960-1686(92)90262-J, 1992.

Rößler, T., Stein, O., Heng, Y., Baumeister, P., and Hoffmann, L.: Trajectory errors of different numerical integration schemes diagnosed with the MPTRAC advection module driven by ECMWF operational analyses, Geosci. Model Dev., 11, 575–592, https://doi.org/10.5194/gmd-11-575-2018, 2018.

Sander, R., Baumgaertner, A., Cabrera-Perez, D., Frank, F., Gromov, S., Grooß, J.-U., Harder, H., Huijnen, V., Jöckel, P., Karydis, V. A., Niemeyer, K. E., Pozzer, A., Riede, H., Schultz, M. G., Taraborrelli, D., and Tauer, S.: The community atmospheric chemistry box model CAABA/MECCA-4.0, Geosci. Model Dev., 12, 1365–1385, https://doi.org/10.5194/gmd-12-1365-2019, 2019.

Sandu, A. and Sander, R.: Technical note: Simulating chemical systems in Fortran90 and Matlab with the Kinetic PreProcessor KPP-2.1, Atmos. Chem. Phys., 6, 187–195, https://doi.org/10.5194/acp-6-187-2006, 2006.

Seinfeld, J. H. and Pandis, S. N.: Atmospheric chemistry and physics: from air pollution to climate change, John Wiley & Sons, 2016.

Stavrakou, T., Müller, J.-F., Boersma, K. F., van der A, R. J., Kurokawa, J., Ohara, T., and Zhang, Q.: Key chemical NO_x sink uncertainties and how they influence top-down emissions of nitrogen oxides, Atmos. Chem. Phys., 13, 9057–9082, https://doi.org/10.5194/acp-13-9057-2013, 2013.

Stein, A. F., Lamb, D., and Draxler, R. R.: Incorporation of detailed chemistry into a three-dimensional Lagrangian–Eulerian hybrid model: application to regional tropospheric ozone, Atmos. Environment, 34, 4361–4372, https://doi.org/10.1016/S1352-2310(00)00204-1, 2000.

Stevenson, D. S., Collins, W. J., Johnson, C. E., and Derwent, R. G.: Intercomparison and evaluation of atmospheric transport in a Lagrangian model (STOCHEM), and an Eulerian model (UM), using 222Rn as a short-lived tracer, Quart. J. Roy. Meteorol. Soc., 124, 2477–2491, https://doi.org/10.1002/qj.49712455115, 1998.

Stohl, A., Forster, C., Frank, A., Seibert, P., and Wotawa, G.: Technical note: The Lagrangian particle dispersion model FLEXPART version 6.2, Atmos. Chem. Phys., 5, 2461–2474, https://doi.org/10.5194/acp-5-2461-2005, 2005.

Stohl, A., Seibert, P., Wotawa, G., Arnold, D., Burkhart, J. F., Eckhardt, S., Tapia, C., Vargas, A., and Yasunari, T. J.: Xenon-133 and caesium-137 releases into the atmosphere from the Fukushima Dai-ichi nuclear power plant: determination of the source term, atmospheric dispersion, and deposition, Atmos. Chem. Phys., 12, 2313–2343, https://doi.org/10.5194/acp-12-2313-2012, 2012.

Tan, Z., Lu, K., Hofzumahaus, A., Fuchs, H., Bohn, B., Holland, F., Liu, Y., Rohrer, F., Shao, M., Sun, K., Wu, Y., Zeng, L., Zhang, Y., Zou, Q., Kiendler-Scharr, A., Wahner, A., and Zhang, Y.: Experimental budgets of OH, HO_2, and RO_2 radicals and implications for ozone formation in the Pearl River Delta in China 2014, Atmos. Chem. Phys., 19, 7129–7150, https://doi.org/10.5194/acp-19-7129-2019, 2019.

Theys, N., De Smedt, I., Yu, H., Danckaert, T., van Gent, J., Hörmann, C., Wagner, T., Hedelt, P., Bauer, H., Romahn, F., Pedergnana, M., Loyola, D., and Van Roozendael, M.: Sulfur dioxide retrievals from TROPOMI onboard Sentinel-5 Precursor: algorithm theoretical basis, Atmos. Meas. Tech., 10, 119–153, https://doi.org/10.5194/amt-10-119-2017, 2017.

Veefkind, J., Aben, I., McMullan, K., Förster, H., de Vries, J., Otter, G., Claas, J., Eskes, H., de Haan, J., Kleipool, Q., van Weele, M., Hasekamp, O., Hoogeveen, R., Landgraf, J., Snel, R., Tol, P., Ingmann, P., Voors, R., Kruizinga, B., Vink, R., Visser, H., and Levelt, P.: TROPOMI on the ESA Sentinel-5 Precursor: A GMES mission for global observations of the atmospheric composition for climate, air quality and ozone layer applications, Remote Sens. Environ., 120, 70–83, https://doi.org/10.1016/j.rse.2011.09.027, the Sentinel Missions - New Opportunities for Science, 2012.

Webster, H. N. and Thomson, D. J.: Using Ensemble Meteorological Data Sets to Treat Meteorological Uncertainties in a Bayesian Volcanic Ash Inverse Modeling System: A Case Study, Grímsvötn 2011, J. Geophys. Res., 127, e2022JD036 469, https://doi.org/10.1029/2022JD036469, 2022.

Wohltmann, I. and Rex, M.: The Lagrangian chemistry and transport model ATLAS: validation of advective transport and mixing, Geosci. Model Dev., 2, 153–173, https://doi.org/10.5194/gmd-2-153-2009, 2009.

Wu, X., Griessbach, S., and Hoffmann, L.: Long-range transport of volcanic aerosol from the 2010 Merapi tropical eruption to Antarctica, Atmos. Chem. Phys., 18, 15 859–15 877, https://doi.org/10.5194/acp-18-15859-2018, 2018.

Wu, X., Griessbach, S., and Hoffmann, L.: Equatorward dispersion of a high-latitude volcanic plume and its relation to the Asian summer monsoon: a case study of the Sarychev eruption in 2009, Atmos. Chem. Phys., 17, 13 439–13 455, https://doi.org/10.5194/acp-17-13439-2017, 2017.